The Astrophysical Journal, 796:84 (14pp), 2014 December 1 doi:10.1088/0004-637X/796/2/84

ALMA IMAGING OF GAS AND DUST IN A GALAXY PROTOCLUSTER AT REDSHIFT 5.3: [C II] EMISSION IN "TYPICAL" GALAXIES AND DUSTY STARBURSTS ≈1 BILLION YEARS AFTER THE BIG BANG

Dominik A. Riechers[1,2], Christopher L. Carilli[3], Peter L. Capak[4], Nicholas Z. Scoville[2], Vernesa Smolčić[5], Eva Schinnerer[6], Min Yun[7], Pierre Cox[8], Frank Bertoldi[9], Alexander Karim[9], and Lin Yan[4]
[1] Department of Astronomy, Cornell University, 220 Space Sciences Building, Ithaca, NY 14853, USA; dr@astro.cornell.edu
[2] Astronomy Department, California Institute of Technology, MC 249-17, 1200 East California Boulevard, Pasadena, CA 91125, USA
[3] National Radio Astronomy Observatory, PO Box O, Socorro, NM 87801, USA
[4] Spitzer Science Center, California Institute of Technology, MC 220-6, 1200 East California Boulevard, Pasadena, CA 91125, USA
[5] University of Zagreb, Physics Department, Bijenička cesta 32, 10002 Zagreb, Croatia
[6] Max-Planck-Institut für Astronomie, Königstuhl 17, D-69117 Heidelberg, Germany
[7] Department of Astronomy, University of Massachusetts, Amherst, MA 01003, USA
[8] ALMA Santiago Central Office, Alonso de Cordova 3107, Vitacura, Santiago, Chile
[9] Argelander-Institut für Astronomie, Universität Bonn, Auf dem Hügel 71, Bonn, D-53121, Germany
Received 2014 April 28; accepted 2014 October 15; published 2014 November 10

ABSTRACT

We report interferometric imaging of [C II]($^2P_{3/2}\rightarrow{}^2P_{1/2}$) and OH($^2\Pi_{1/2}$ $J = 3/2\rightarrow 1/2$) emission toward the center of the galaxy protocluster associated with the $z = 5.3$ submillimeter galaxy (SMG) AzTEC-3, using the Atacama Large (sub)Millimeter Array (ALMA). We detect strong [C II], OH, and rest-frame 157.7 μm continuum emission toward the SMG. The [C II]($^2P_{3/2}\rightarrow{}^2P_{1/2}$) emission is distributed over a scale of 3.9 kpc, implying a dynamical mass of $9.7\times10^{10}\,M_\odot$, and a star formation rate (SFR) surface density of $\Sigma_{\rm SFR} = 530\,M_\odot\,{\rm yr}^{-1}\,{\rm kpc}^{-2}$. This suggests that AzTEC-3 forms stars at $\Sigma_{\rm SFR}$ approaching the Eddington limit for radiation pressure supported disks. We find that the OH emission is slightly blueshifted relative to the [C II] line, which may indicate a molecular outflow associated with the peak phase of the starburst. We also detect and dynamically resolve [C II]($^2P_{3/2}\rightarrow{}^2P_{1/2}$) emission over a scale of 7.5 kpc toward a triplet of Lyman-break galaxies with moderate UV-based SFRs in the protocluster at ∼95 kpc projected distance from the SMG. These galaxies are not detected in the continuum, suggesting far-infrared SFRs of <18–54 $M_\odot\,{\rm yr}^{-1}$, consistent with a UV-based estimate of 22 $M_\odot\,{\rm yr}^{-1}$. The spectral energy distribution of these galaxies is inconsistent with nearby spiral and starburst galaxies, but resembles those of dwarf galaxies. This is consistent with expectations for young starbursts without significant older stellar populations. This suggests that these galaxies are significantly metal-enriched, but not heavily dust-obscured, "normal" star-forming galaxies at $z > 5$, showing that ALMA can detect the interstellar medium in "typical" galaxies in the very early universe.

Key words: cosmology: observations – galaxies: active – galaxies: formation – galaxies: high-redshift – galaxies: starburst – radio lines: galaxies

Online-only material: color figures

1. INTRODUCTION

The first massive galaxies in the universe are expected to rapidly grow in the most massive dark matter halos at early cosmic epochs (e.g., Efstathiou & Rees 1988; Kauffmann et al. 1999). Such high overdensities in the dark matter distribution are expected to be associated accordingly with overdensities of baryonic matter, and thus, protoclusters of galaxies (e.g., Springel et al. 2005). The bulk of the stellar mass in the most massive galaxies in these halos likely grows in short, episodic bursts associated with major gas-rich mergers and/or peak phases of gas accretion from the intergalactic medium (e.g., Blain et al. 2004). These starbursts, in turn, may significantly enrich the galaxy's environment with heavy elements through winds and outflows (e.g., McKee & Ostriker 1977; Sturm et al. 2011; Spoon et al. 2013).

The identification of massive starburst galaxies at the highest redshifts may be the most promising way to find such exceptional cosmic environments. The most intense starbursts are commonly enshrouded by dust, rendering them difficult to identify at rest-frame UV/optical wavelengths (e.g., Smail et al. 1997; Hughes et al. 1998; Chapman et al. 2003). The dust-absorbed stellar light is re-emitted at rest-frame far-infrared (FIR) wavelengths, making such galaxies bright in the observed-frame (sub-)millimeter at high redshift (so-called submillimeter galaxies, or SMGs; see review by Blain et al. 2002).

We have recently identified AzTEC-3, a gas-rich SMG at $z = 5.3$ (Riechers et al. 2010, hereafter R10; Capak et al. 2011, hereafter C11) in the AzTEC 1.1 mm study of the Cosmic Evolution Survey (COSMOS) field (Scoville et al. 2007; Scott et al. 2008). AzTEC-3 has a relatively compact (<4 kpc radius), highly excited molecular gas reservoir of $5.3\times10^{10}\,M_\odot$ (determined through the detection of three CO lines; R10), which gets converted into stars at a rate of $>1000\,M_\odot\,{\rm yr}^{-1}$ (C11). Its current stellar mass is estimated to be $M_\star = (1.0\pm0.2)\times10^{10}\,M_\odot$ (C11).[10]

The environment of AzTEC-3 represents one of the most compelling pieces of observational evidence for the hierarchical picture of massive galaxy evolution. The massive starburst galaxy is associated with a >11-fold overdense structure of "normal" star-forming galaxies at the same redshift[11] that extends out to >13 Mpc on the sky, with >10 galaxies within the central (co-moving) ∼2 Mpc radius region (C11). The protocluster galaxies alone (including the SMG) place a lower limit

[10] These estimates depend on the assumed stellar initial mass function; see, e.g., Dwek et al. (2011).
[11] Based on photometric redshifts and several spectroscopic confirmations (C11).

of $4\times10^{11}\ M_{\odot}$ on the mass of dark and luminous matter associated with this region (C11). However, our current understanding of this exceptional cosmic environment is dominantly based on the rest-frame UV/optical properties of all galaxies except the SMG, and thus, may be incomplete due to lack of information on the gas and dust in their interstellar media (ISM).

Here we report 158 μm [C II]($^2P_{3/2}\rightarrow{}^2P_{1/2}$), 163 μm OH($^2\Pi_{1/2}$ $J=3/2\rightarrow1/2$), and rest-frame 157.7 μm dust continuum imaging toward the center of the galaxy protocluster associated with the $z=5.3$ SMG AzTEC-3 with ALMA. The [C II]($^2P_{3/2}\rightarrow{}^2P_{1/2}$) line is the dominant cooling line of the cold[12] ISM in star-forming galaxies (where it can carry up to 1% of $L_{\rm FIR}$; e.g., Israel et al. 1996), typically much brighter than CO lines, and traces regions of active star formation (photon-dominated regions, or PDRs) and the cold, neutral atomic medium (CNM; e.g., Stacey et al. 1991). It thus is an ideal tracer for the distribution, dynamics, and enrichment of the ISM out to the most distant galaxies, but it was only detected in some of the most luminous quasars and starburst galaxies in the past (e.g., Maiolino et al. 2005, 2009; Walter et al. 2009; Stacey et al. 2010; Wagg et al. 2010; Valtchanov et al. 2011; Riechers et al. 2013; Wang et al. 2013)—i.e., systems that are much more extreme than typical protocluster galaxies. Previous searches for [C II] emission in typical and/or ultraviolet-luminous galaxies at $z>5$ have been unsuccessful (e.g., Walter et al. 2012b; Kanekar et al. 2013; Ouchi et al. 2013; Gonzalez-Lopez et al. 2014), and it is important to understand what role environment may play for the detectability of such objects. The far-infrared lines of the OH radical are important for the H_2O chemistry and cooling budget of star-forming regions, and they are critical tracers of molecular outflows (e.g., Sturm et al. 2011; Gonzalez-Alfonso et al. 2012), but OH was only detected in a single galaxy at cosmological distances to date (Riechers et al. 2013). We use a concordance, flat ΛCDM cosmology throughout, with $H_0=71\ {\rm km\,s^{-1}\,Mpc^{-1}}$, $\Omega_{\rm M}=0.27$, and $\Omega_{\Lambda}=0.73$ (Spergel et al. 2003, 2007).

2. OBSERVATIONS

We observed the [C II]($^2P_{3/2}\rightarrow{}^2P_{1/2}$) transition line ($\nu_{\rm rest}=1900.5369$ GHz, redshifted to 301.72 GHz, or 994 μm, at $z=5.299$), using ALMA. Observations were carried out with 16–24 usable 12 m antennas under good 870 μm weather conditions (precipitable water vapor of 0.64–1.76 mm) for 4 tracks in the cycle 0 extended configuration (longest baseline: 402 m) between 2012 April 11 and May 17, and for 1 track in the cycle 0 compact configuration[13] (shortest baseline: 21 m) on 2012 November 18 (three additional tracks were discarded due to poor data quality). This resulted in 125 minute on-source time, which was evenly split over two (slightly overlapping) pointings (primary beam FWHM diameter at 994 μm: 20″). The nearby radio quasar J1058+015 was observed regularly for pointing, bandpass, amplitude and phase calibration. Fluxes were derived relative to Titan or Callisto. We estimate the overall accuracy of the calibration to be accurate within ∼20%.

The correlator was set up to target two spectral windows of 1.875 GHz bandwidth each at 0.488 MHz (0.48 km s^{-1}) resolution (dual polarization) in each sideband. The [C II] line was centered in one spectral window in the upper sideband. The other three windows were used to measure the continuum emission ∼2 GHz above and ∼10–12 GHz below the line frequency. This setup also covered the 163 μm OH($^2\Pi_{1/2}$ $J=3/2\rightarrow1/2$) line (components at $\nu_{\rm rest}=1834.74735$ and 1837.81682 GHz, redshifted to 291.27597 and 291.76327 GHz at $z=5.299$),[14] as well as the CO($J=16\rightarrow15$) line ($\nu_{\rm rest}=1841.345506$ GHz, redshifted to 292.32346 GHz), in the lower sideband.

The Astronomical Image Processing System (AIPS) and Common Astronomy Software Applications (CASA) packages were used independently for data reduction and analysis to better quantify potential uncertainties in the calibration. Primary beam-corrected mosaics were created using the FLATN task in AIPS. All data were mapped using the CLEAN algorithm with "natural" weighting, resulting in a synthesized beam size of $0\farcs63\times0\farcs55$ at the redshifted [C II] line frequencies ($0\farcs63\times0\farcs56$ when averaging over the three [C II] line-free spectral windows). The final rms noise when averaging over all spectral windows (i.e., over a total of 7.5 GHz of bandwidth) is ∼50 μJy beam^{-1} in the phase centers of both pointings, and scales as expected for thermal noise in narrower frequency bins (see figure captions).[15] This sensitivity level is consistent with standard theoretical estimates when assuming the atmospheric conditions and instrument configurations used for our observations.

3. RESULTS

3.1. Continuum

We have detected 1.0 mm continuum emission toward the $z=5.3$ SMG AzTEC-3 (Figure 1). From two-dimensional Gaussian fitting to a data set averaged over the line-free spectral windows, we find a continuum flux density of 6.20 ± 0.25 mJy (Table 1) and a deconvolved continuum source size of $0\farcs40^{+0\farcs04}_{-0\farcs04}\times0\farcs17^{+0\farcs08}_{-0\farcs17}$ (2.5×1.1 kpc^2 at $z\simeq5.3$; Table 2).[16]

The two pointings also covered five Lyman-break galaxies with photometric redshifts close to (or colors consistent with) $z=5.3$, with COSMOS optical IDs 1447523, 1447526 (Ilbert et al. 2009; "LBG-2" and "LBG-3" in the following; ∼1.″7 northeast and ∼2.″2 northwest of AzTEC-3), and 1447524 (a triple of sources ∼15″ southeast of AzTEC-3, targeted by the second pointing; "LBG-1" below and in Figure 1; see C11 for more details on the source identifications). Besides color information, LBG-1 has an optical spectroscopic redshift of $z_{\rm spec}=5.300$ that is likely valid for all of its three components (LBG-1a, LBG-1b, and LBG-1c below), and LBG-3 has a photometric redshift of $z_{\rm phot}=5.269$ (C11). No 1.0 mm continuum emission is detected toward any of these galaxies, with 3σ upper limits

[12] Cold here means $\ll10^4$ K, i.e., in the regime where dust cooling through (far-)infrared emission is prevalent, and below the regime where cooling through hydrogen lines dominates.

[13] Given the increased number of antennas available, this configuration also contained antennas on longer baselines than the originally advertised 125 m.

[14] These components are due to a [$P=(-)\rightarrow(+)$, $P=(+)\rightarrow(-)$] Λ-doublet in the orbital angular momentum of the OH radical. Each P component of the $J=3/2\rightarrow1/2$ transition consists of an unresolved F triplet of transitions due to hyperfine structure splitting of the levels (see, e.g., Genzel et al. 1985; Cesaroni & Walmsley 1991).

[15] A narrow, limited frequency range at 301.8 GHz (corresponding to approximately −70 km s^{-1} on the velocity scale used throughout the paper) is affected by a narrow atmospheric feature, which causes the sensitivity to be $\lesssim$15%–20% worse than nominal. The feature is narrow compared to all detected emission lines. Also, it is offset from virtually all line emission in LBG-1, and from the center of the [C II] line in AzTEC-3. This feature may be responsible for the slightly higher apparent rms noise level in the rightmost panel of Figure 8. Other known atmospheric features in the frequency range of our observations are very weak, and affect the sensitivity at a few percent level at most, and all lie outside the spectral windows that contain the [C II] and OH emission.

[16] Errors are determined as described by Condon (1997).

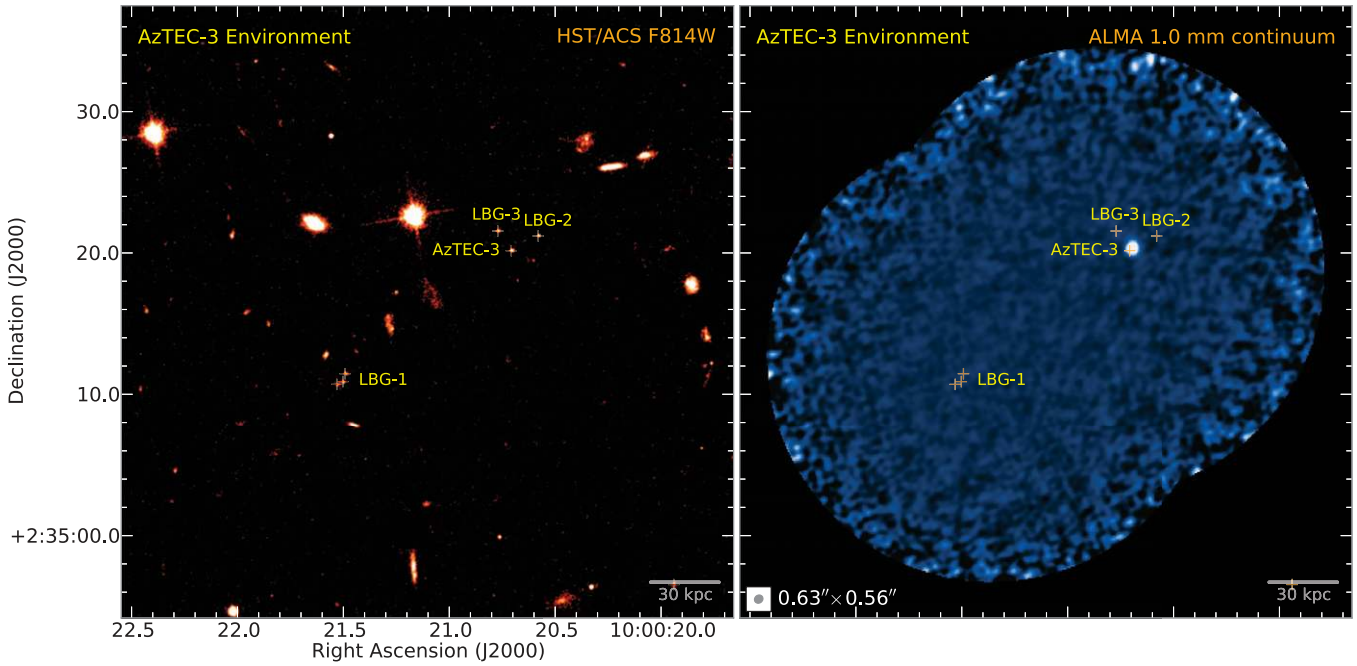

Figure 1. *HST*/ACS F814W (left) and ALMA 1.0 mm continuum image (rest-frame 157.7 μm; right) of the targeted region. Two pointings were observed to cover AzTEC-3 at $z = 5.3$ and five candidate companion Lyman-break galaxies (positions are indicated by plus signs; LBG-1 contains three components). The 1.0 mm continuum image was obtained by averaging the three [C II] line-free spectral windows (corrected for primary beam attenuation). The rms at the phase centers is $\sim$58 μJy beam^{-1}, and increases outwards due to the primary beam response. The synthesized beam size of $0\farcs63 \times 0\farcs56$ is indicated in the bottom left corner of the right panel.

(A color version of this figure is available in the online journal.)

Table 1
[C II] and Continuum Properties of Sources in the $z = 5.3$ Protocluster

Target	Redshift	$S_{\rm C\,II}$ (mJy)	d$v_{\rm C\,II}$ (km s^{-1})	$I_{\rm C\,II}$ (Jy km s^{-1})	$L'_{\rm C\,II}$ (10^{10} K km s^{-1} pc^2)	$L_{\rm C\,II}$ (10^9 $L_\odot$)	$S_{1.0\,\rm mm}$ (mJy)	$\log_{10}(L_{\rm C\,II}/L_{\rm FIR})$
AzTEC-3	5.2988 ± 0.0001	18.4 ± 0.5	421 ± 19	8.21 ± 0.29	3.05 ± 0.11	6.69 ± 0.23	6.20 ± 0.25	–3.40
LBG-1	5.2950 ± 0.0002	8.99 ± 0.73	218 ± 24	2.08 ± 0.18	0.77 ± 0.07	1.69 ± 0.15	<0.45	$>(-2.50)$
							<0.15–0.24[a,b]	$>(-2.03)$–(-2.22)[c]
LBG-2				<0.21[b,d]	<0.08[b,d]	<0.17[b,d]	<0.24[b]	
LBG-3				<0.21[b,d]	<0.08[b,d]	<0.17[b,d]	<0.24[b]	

Notes. All quoted upper limits are 3σ.
[a] Individual limits for subcomponents LBG-1a, LBG-1b, and LBG-1c.
[b] Point source limits in mJy beam^{-1}, Jy beam^{-1} km s^{-1}, or equivalent.
[c] Assuming that the far-infrared continuum emission is not resolved by our observations.
[d] Assuming the same line width and redshift as measured for LBG-1. Assuming an average or median of the line width of the subcomponents of LBG-1 would result in $\sim$10%–15% lower limits. We consider this difference in limits negligible compared to other sources of uncertainty.

Table 2
Derived [C II] and Continuum Properties

Target	d([C II])	$d_{\rm phys}$([C II]) (kpc × kpc)	d(FIR)	$d_{\rm phys}$(FIR) (kpc × kpc)	$\rm SFR_{FIR}$[a] ($M_\odot$ yr^{-1})	$\Sigma_{\rm SFR}$ ($M_\odot$ yr^{-1} kpc^{-2})	$M_{\rm dyn}^{\rm [C\,II]b}$ (10^{10} $M_\odot$)
AzTEC-3	$0\farcs63^{+0\farcs09}_{-0\farcs09} \times 0\farcs34^{+0\farcs10}_{-0\farcs15}$	3.9 × 2.1	$0\farcs40^{+0\farcs04}_{-0\farcs04} \times 0\farcs17^{+0\farcs08}_{-0\farcs17}$	2.5 × 1.1	1100	530	9.7
LBG-1	$1\farcs21^{+0\farcs41}_{-0\farcs69} \times 0\farcs95^{+0\farcs68}_{-0\farcs37}$	7.5 × 5.9	*undetected*	···	<18–54[c]	···	5.0
LBG-2	*undetected*	···	*undetected*	···	<28[d]	···	···
LBG-3	*undetected*	···	*undetected*	···	<28[d]	···	···

Notes.
[a] Determined from $L_{\rm FIR}$, assuming a Chabrier (2003) initial mass function.
[b] Derived assuming an isotropic virial estimator (e.g., Engel et al. 2010), and the galaxy size along the major axis.
[c] The lower of the limits assumes that all $\rm SFR_{FIR}$ is concentrated toward one component, the higher limit assumes that it is spatially resolved and spread over all components (LBG-1a, LBG-1b, and LBG-1c).
[d] Point source limits, assuming the same redshift and SED shape as for LBG-1.

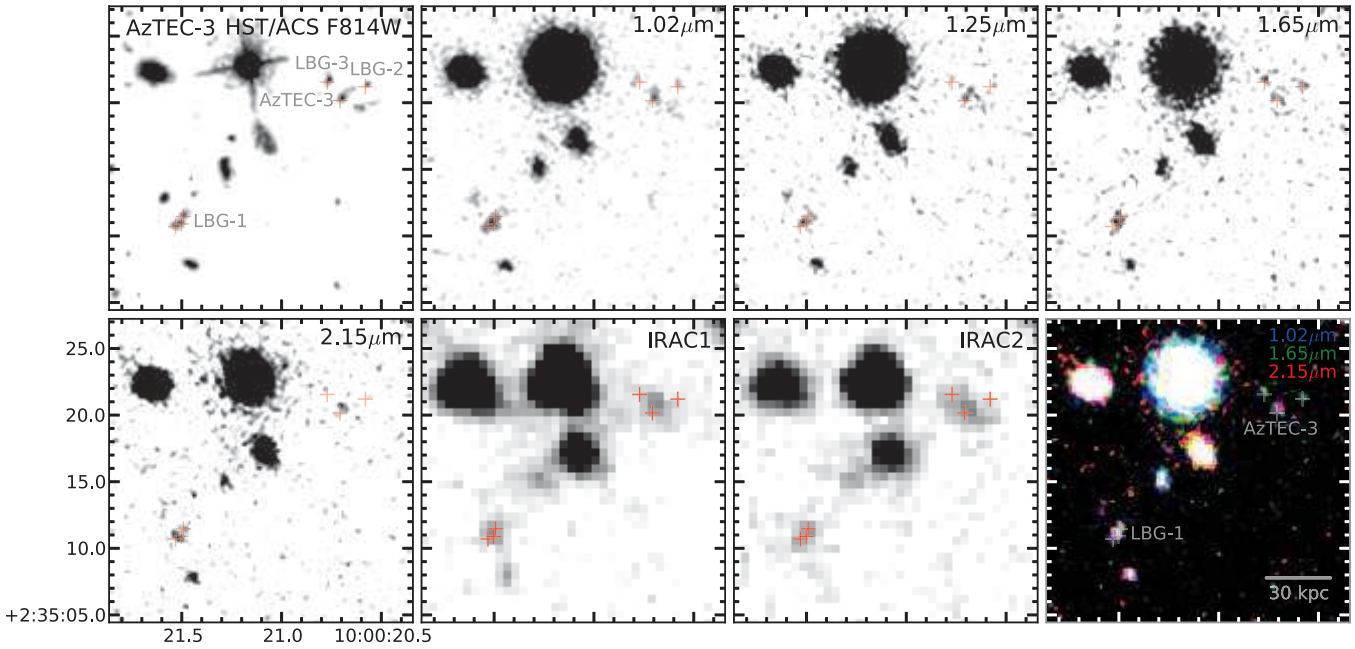

Figure 2. Images of the field observed with ALMA in the *HST*/ACS *i* (F814W), UltraVISTA *Y*, *J*, *H*, *Ks* (1.02, 1.25, 1.65, 2.15 μm), *Spitzer* IRAC1 (3.6 μm), and IRAC2 (4.5 μm) bands, and *YHKs* three-color image (Scoville et al. 2007; McCracken et al. 2012; Sanders et al. 2007). Adaptive smoothing has been applied to the *HST*/ACS image. The plus signs indicate the same positions as in Figure 1.

(A color version of this figure is available in the online journal.)

of 0.24 mJy beam^{-1} for LBG-2 and LBG-3 (conservative limits are quoted due to potential sidelobe residuals from AzTEC-3), and 0.45 mJy for LBG-1 (or 0.15–0.24 mJy beam^{-1} for the three LBG subcomponents when accounting for potential source overlap at the current spatial resolution). Based on their small sizes in *HST*/ACS F814W imaging data (Figure 1), we assume in the following that LBG-2 and LBG-3 are spatially unresolved by our ALMA observations. Given the spatial separation of the three components of LBG-1 (Figure 1) and the spatial extent of the [C II]($^2P_{3/2}\rightarrow{}^2P_{1/2}$) emission (see below), we assume that the continuum emission in this source is resolved over $\sim$3 beams for the above estimate. We adopt this spatially integrated limit (rather than more sensitive limits for individual or stacked LBG components) in the following, to enable comparison with existing resolution-limited photometry at other wavelengths (see, e.g., Figure 2).

3.2. [C II]($^2P_{3/2}\rightarrow{}^2P_{1/2}$) Line Emission

We have detected strong [C II]($^2P_{3/2}\rightarrow{}^2P_{1/2}$) line emission toward AzTEC-3 (Figure 3). From two-dimensional Gaussian fitting to the line emission, we find a deconvolved [C II] source size of $0\farcs63^{+0\farcs09}_{-0\farcs09} \times 0\farcs34^{+0\farcs10}_{-0\farcs15}$ (3.9 × 2.1 kpc^2; Table 2). The [C II] emission is compact over the entire velocity range, without evidence for a significant shift in the centroid position between velocity channels (Figures 3–5). The [C II] peak position is consistent with those of the CO and FIR continuum emission (R10), as well as with the peak of the optical emission longward of observed-frame $\sim$2 μm (Figure 2). There is tentative evidence in different velocity intervals for emission that may extend beyond the central, compact component that dominates the [C II] emission, but only at low flux density levels. The most prominent of these features is a faint [C II] emission component in the blue line wing that extends northeast from the center of the galaxy (Figure 6, left). This component could correspond to a tidal feature, a close galaxy companion in a minor merger event, or a [C II] outflow (or inflow). A similar, but less significant feature is seen in the red [C II] line wing (Figure 6, right). Observations at higher spatial resolution are required to further resolve the detailed structure of the interstellar medium in this massive starburst galaxy.

We have also detected [C II]($^2P_{3/2}\rightarrow{}^2P_{1/2}$) emission toward the triple Lyman-break galaxy system LBG-1 (Figure 7). The emission is spatially resolved on a scale of $1\farcs21^{+0\farcs41}_{-0\farcs69} \times 0\farcs95^{+0\farcs68}_{-0\farcs37}$ (7.5 × 5.9 kpc^2; Table 2), covering all three optical emission regions (LBG-1a, LBG-1b, and LBG-1c; Figure 7). The [C II] emission thus is clearly resolved toward the three components, which is seen more prominently in different velocity bins along the line emission (Figures 7 and 8). No [C II]($^2P_{3/2}\rightarrow{}^2P_{1/2}$) emission is detected toward LBG-2 or LBG-3.

The [C II]($^2P_{3/2}\rightarrow{}^2P_{1/2}$) line parameters and redshifts for all detected galaxies were determined with four parameter Gaussian fits to the line and continuum emission spectra (Table 1). The [C II] emission in AzTEC-3 has a peak flux density of 18.4 ± 0.5 mJy at a line FWHM of 421 ± 19 km s^{-1}, corresponding to an integrated line flux of 8.21 ± 0.29 Jy km s^{-1}, and peaks at a redshift of $z = 5.2988 \pm 0.0001$ (Figure 9, left). The [C II] emission in LBG-1 has a peak flux density of 8.99 ± 0.73 mJy at a line FWHM of 218 ± 24 km s^{-1}, corresponding to an integrated line flux of 2.08 ± 0.18 Jy km s^{-1}, and peaks at a central redshift of $z = 5.2950 \pm 0.0002$ (Figure 10, left). The central velocities and line shapes of the [C II] emission are different at the optical positions of the three regions (Figure 10, middle). The three components LBG-1a, b, and c peak at velocities of −49 ± 18, −3 ± 12, and +25 ± 16 km s^{-1} relative to the central redshift, with line FWHM of 93 ± 32, 152 ± 29, and 250 ± 41 km s^{-1}, respectively (Table 3; Figure 10, middle). LBG-1a is the faintest and narrowest component, and thus, does not show a clearly spatially separated peak in the velocity-integrated [C II] map (Figure 7). However, the [C II] line emission clearly extends toward LBG-1a in maps of narrower

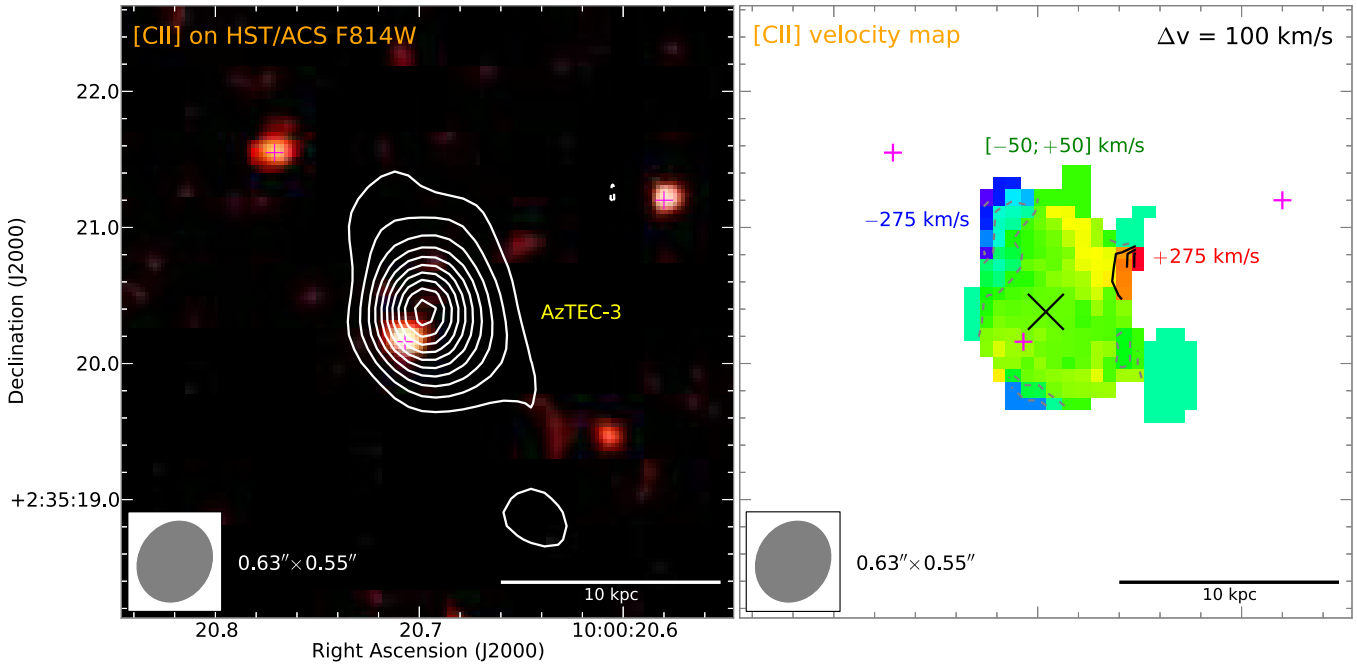

Figure 3. Velocity-integrated ALMA [C II]($^2P_{3/2}\rightarrow{}^2P_{1/2}$) contours overlaid on the *HST*/ACS F814W image (left) and [C II]($^2P_{3/2}\rightarrow{}^2P_{1/2}$) velocity map (right) toward AzTEC-3. Continuum emission has been subtracted from all maps. Left: the map is averaged over 468.75 MHz (466 km s^{-1}). Contours start at $\pm4\sigma$ and are in steps of 4σ ($1\sigma = 200\,\mu$Jy beam^{-1} at the phase center). The synthesized beam size of $0\farcs63 \times 0\farcs55$ is indicated in the bottom left corners. The plus signs indicate the same positions as in Figure 1. The [C II] peak position (black cross in right panel) is consistent with those of the CO and FIR continuum emission (R10). Right: First moment map (i.e., intensity weighted mean velocity image) of the [C II] velocity structure. The colors indicate the velocity gradient. Contours are shown in steps of 100 km s^{-1}, with dashed (solid) contours showing blueshifted (redshifted) emission relative to zero velocity. The velocity scale is relative to $z = 5.2988$.

(A color version of this figure is available in the online journal.)

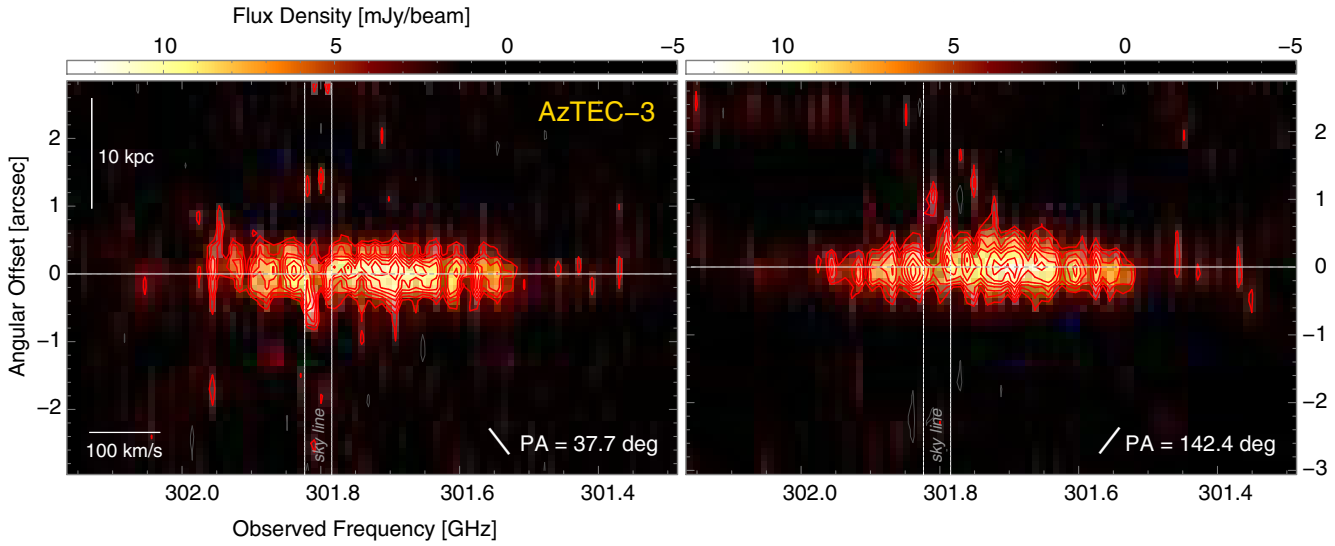

Figure 4. ALMA [C II]($^2P_{3/2}\rightarrow{}^2P_{1/2}$) position–velocity ($p$–$v$) diagrams of AzTEC-3. Continuum emission has been subtracted from the data cube. Left: p–v diagram along an axis with a position angle of 37.°7 (direction as indicated by the inclined, short solid line), which connects the line centroid with the peak to the northeast seen in the blue velocity range in Figure 6. Right: p–v diagram along an axis perpendicular to that in the left panel (position angle of 142.°4). Data are shown at a spectral resolution of 9.77 MHz (~10 km s^{-1}). The spatial pixel scale is the same as in Figure 3. Contours are shown in steps of 1σ, starting at $\pm3\sigma$. Negative contours are shown as thin gray lines. The dotted lines indicate a narrow frequency range where the sensitivity may be reduced by a few percent to $\lesssim$15%–20% relative to the nominal value due to a weak atmospheric absorption feature (see discussion in Section 2).

(A color version of this figure is available in the online journal.)

velocity bins (Figure 8). No [C II] emission is detected toward LBG-2 and LBG-3 down to 3σ limits of 0.21 and 0.21 Jy km s^{-1}, assuming the same line width and redshift as measured for LBG-1. We also stacked the spectra of LBG-2 and LBG-3, which did not result in a detection either (Figure 10, right). We caution that this stack only provides a $\sqrt{2}$ deeper [C II] limit if these galaxies are at a common redshift.

3.3. OH and CO Line Emission

We have successfully detected the OH($^2\Pi_{1/2}\,J = 3/2\rightarrow 1/2$) doublet toward AzTEC-3 (Figure 9, middle). We measure peak flux densities of 1.46 ± 0.22 and 2.07 ± 0.22 mJy for the two components of the Λ-doublet, at a common line FWHM of 384 ± 43 km s^{-1} for each component. This corresponds

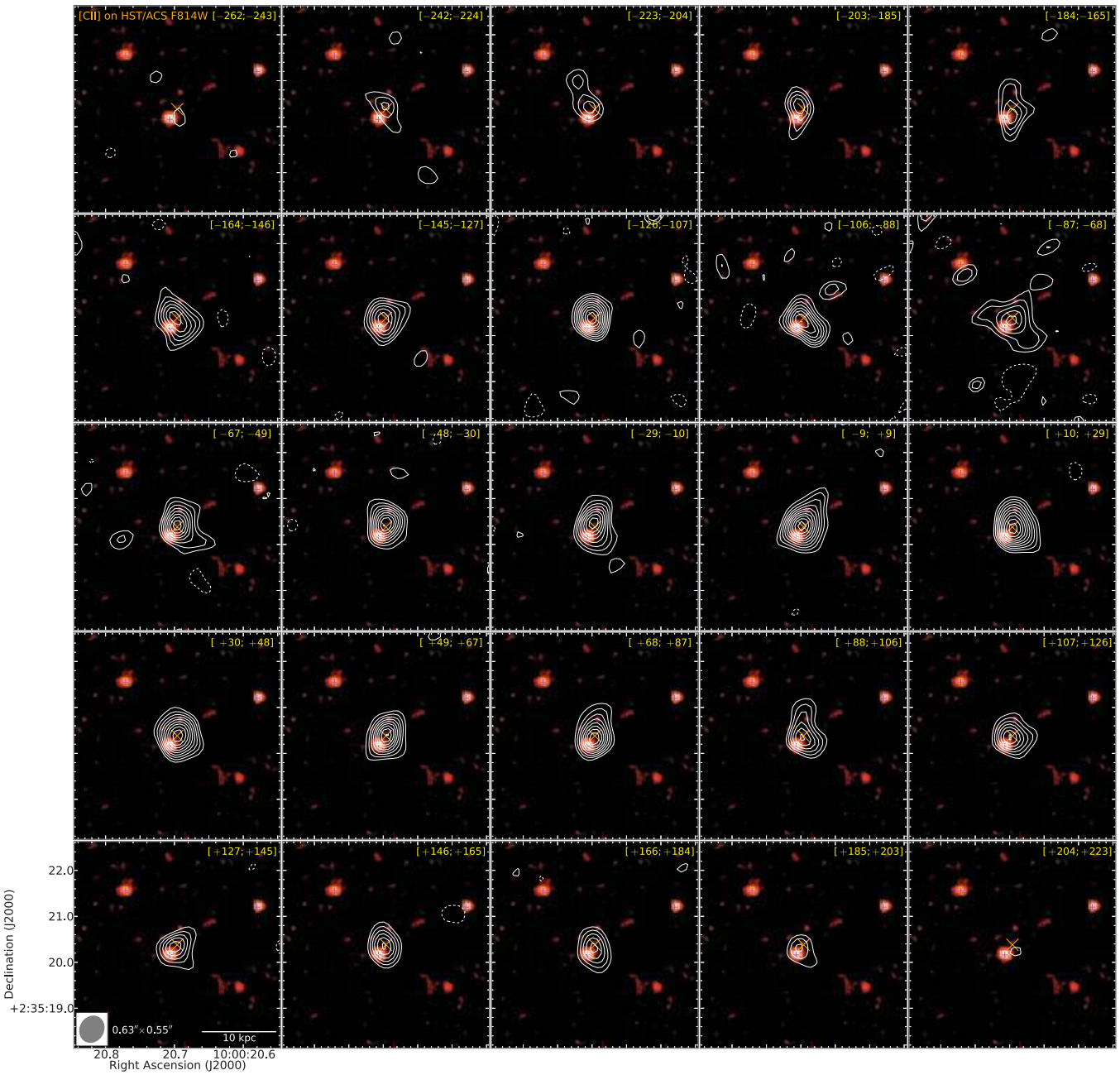

Figure 5. ALMA [C II]($^2P_{3/2}\rightarrow{}^2P_{1/2}$) velocity channel contours overlaid on the *HST*/ACS F814W image toward AzTEC-3. Velocity channels are averaged over ∼19.53 MHz (∼19 km s^{-1}). Contours start at ±3σ and are in steps of 1σ (1σ = 974 μJy beam^{-1} at the phase center). The noise close to −70 km s^{-1} is slightly higher due to a weak atmospheric absorption feature (see Section 2). Velocity ranges in km s^{-1} are indicated in the top right corner of each panel. The synthesized beam size is the same as in Figure 3. The velocity scale is the same as in Figure 3. The crosses and plus signs indicate the same positions as in Figure 3.

(A color version of this figure is available in the online journal.)

to an integrated line flux of 1.44 ± 0.13 Jy km s^{-1} (Table 4). This 163 μm OH feature thus has a higher line flux than any CO lines detected in this source, carrying almost 20% of the flux of the [C II]($^2P_{3/2}\rightarrow{}^2P_{1/2}$) line. The central velocity of the feature is shifted by –109 ± 19 km s^{-1} relative to the [C II] line. This may indicate that the OH emission is associated with an outflow, but better sensitivity and higher spatial resolution observations are required to further investigate such a scenario.

Our observations also covered the CO(J = 16→15) line in AzTEC-3, but no emission was detected (Figure 9, right). We place a 3σ limit of <0.22 Jy km s^{-1} on the strength of the line, assuming the same width as that of the CO(J = 5→4) line (487 ± 58 km s^{-1}; R10). This limit is 4–6 × lower than the fluxes measured in the CO(J = 5→4) and CO(J = 6→5) lines, suggesting that no strong component with high CO excitation is present.

Based on the [C II] redshift, we have used a recent data set (PI: Riechers) from the Karl G. Jansky Very Large Array (VLA) to search for CO(J = 2→1) line emission toward LBG-1. We do not detect any signal down to an approximate 3σ limit of <0.03 Jy km s^{-1}, assuming the same width and redshift as for the [C II] line (Figure 11; these data will be described in detail in a future publication, D. A Riechers et al. 2015, in preparation). Given this non-detection, we do not consider the limits on the OH($^2\Pi_{1/2}$ J = 3/2→1/2) and CO(J = 16→15) lines from

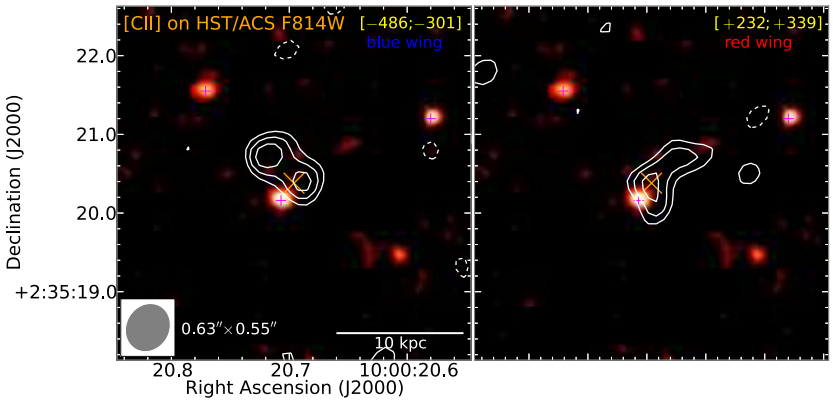

Figure 6. ALMA [C II]($^2P_{3/2}\rightarrow{}^2P_{1/2}$) velocity channel contours of the line wings overlaid on the *HST*/ACS F814W image toward AzTEC-3. Velocity channels in the left and right panels are averaged over ∼185.55 and 107.42 MHz (∼184 and 107 km s^{-1}), respectively. Contours start at ±3σ and are in steps of 1σ (1σ = 316 and 415 μJy beam^{-1} at the phase center). Velocity ranges in km s^{-1} are indicated in the top right corner of each panel. The synthesized beam size is the same as in Figure 3. The velocity scale is the same as in Figure 3. The crosses and plus signs indicate the same positions as in Figure 3.

(A color version of this figure is available in the online journal.)

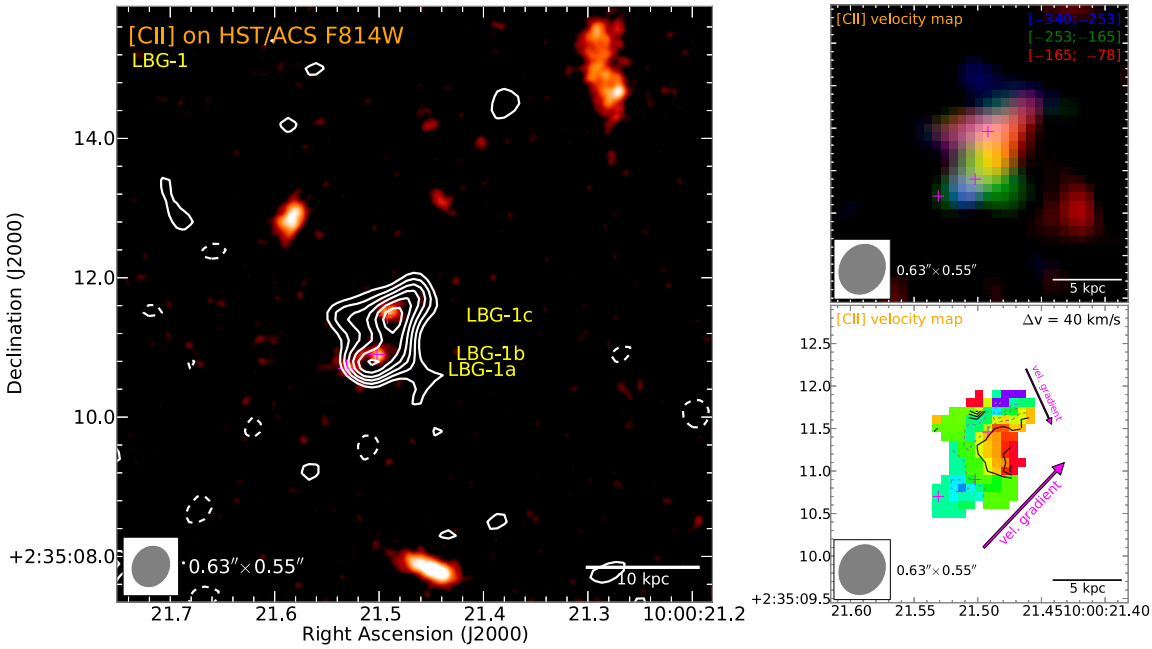

Figure 7. Velocity-integrated ALMA [C II]($^2P_{3/2}\rightarrow{}^2P_{1/2}$) contours overlaid on the *HST*/ACS F814W image (left) and [C II]($^2P_{3/2}\rightarrow{}^2P_{1/2}$) velocity maps (right) toward LBG-1. Left: the map is averaged over ∼332 MHz (330 km s^{-1}). Contours start at ±3σ and are in steps of 1σ (1σ = 236 μJy beam^{-1} at the phase center). The synthesized beam size is the same as in Figure 3. The plus signs indicate the same positions as in Figure 1. Right: color-encoded velocity structure and first moment map of the [C II] emission. The channel maps in the top right panel include emission above 3σ significance (1σ = 460 μJy beam^{-1} at the phase center). The colors indicate different velocity bins. Velocity ranges in km s^{-1} for each color are indicated in the top right corner. The velocity scale is the same as in Figure 3. The colors in the first moment map (bottom right) indicate the velocity gradient. Contours are shown in steps of 40 km s^{-1}, with dashed (solid) contours showing blueshifted (redshifted) emission relative to the central velocity of LBG-1 at z = 5.2950. The arrows indicate the general directions (blue- to redshifted) of the two strongest velocity gradients.

(A color version of this figure is available in the online journal.)

the ALMA data to be constraining for this source. Given the nondetections of [C II], we do not extract limits on these lines for LBG-2 and LBG-3 either.

3.4. Spectral Energy Distribution

3.4.1. AzTEC-3

To determine the spectral energy distribution (SED) properties of AzTEC-3 after including the new constraints from ALMA, we have fit modified black-body (MBB) models to the continuum data between observed-frame 100 μm and 8.2 mm (R10; C11; Huang et al. 2014; Smolčić et al. 2014). The MBB is joined to a $\nu^{-\alpha}$ power law on the blue side of the SED peak.

We used an affine-invariant Markov Chain Monte-Carlo (MCMC) approach, employing the method described by Riechers et al. (2013) and Dowell et al. (2014).[17] We first fit optically thin models, using α, the dust temperature $T_{\rm dust}$, the power law slope of the dust extinction curve β, and a normalization factor (for which we elect the observed-frame 500 μm flux density) as fitting parameters. A weak Gaussian prior of

[17] https://github.com/aconley/mbb_emcee

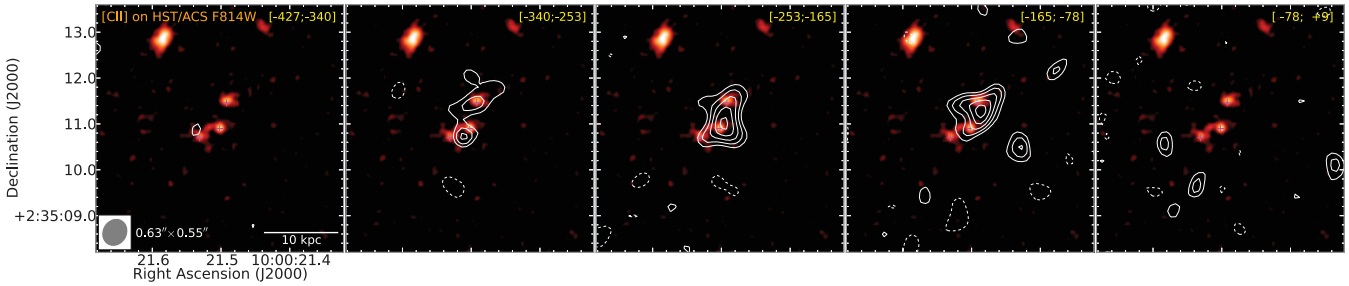

Figure 8. ALMA [C II]($^2P_{3/2}\rightarrow{}^2P_{1/2}$) velocity channel contours overlaid on *HST*/ACS F814W image toward LBG-1. Velocity channels are averaged over 87.89 MHz (87 km s^{-1}). Contours start at $\pm3\sigma$ and are in steps of 1σ ($1\sigma = 460$ μJy beam^{-1} at the phase center). The noise in the rightmost channel is slightly higher due to a weak atmospheric absorption feature (see Section 2). Velocity ranges in km s^{-1} are indicated in the top right corner of each panel. The synthesized beam size is the same as in Figure 7. The velocity scale is the same as in Figure 7. The plus signs indicate the same positions as in Figure 7.

(A color version of this figure is available in the online journal.)

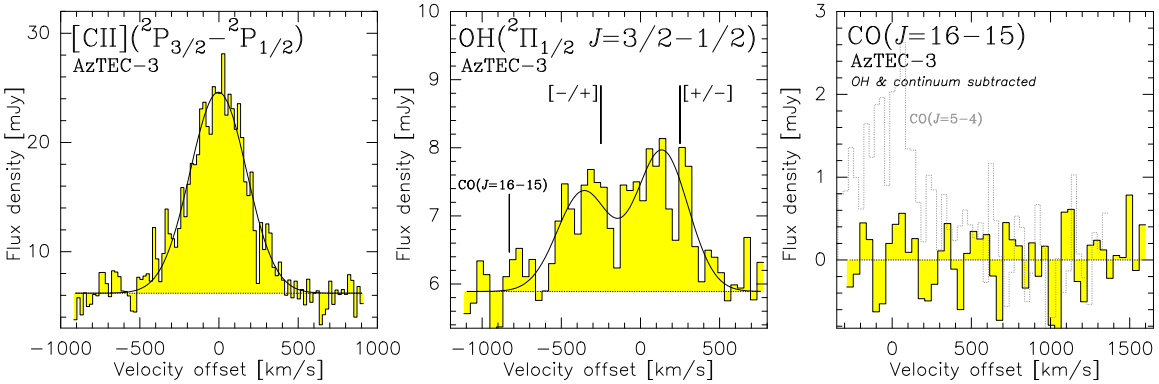

Figure 9. ALMA spectra of the [C II]($^2P_{3/2}\rightarrow{}^2P_{1/2}$) (left), OH($^2\Pi_{1/2}$ $J = 3/2\rightarrow1/2$) (middle), and CO($J = 16\rightarrow15$) (right) lines toward AzTEC-3. Spectra (histograms) are shown at resolutions of 20 MHz (20 km s^{-1}; [C II]) or 40 MHz (41 km s^{-1}; OH and CO). The velocity scales are relative to $z = 5.2988$. Detected lines are shown along with Gaussian fits to the line emission (black curves). In the case of OH, zero velocity corresponds to the central frequency between the P components of the Λ doublet. The [+/−] and [−/+] labels at ±249 km s^{-1} indicate the P components of the Λ doublet (i.e., $J^P = 3/2^+\rightarrow1/2^-$ and $3/2^-\rightarrow1/2^+$, respectively). Due to the narrow splitting ($\sim$14 and 2 MHz observed-frame, respectively), labels for hyperfine structure splitting of the P components are omitted for clarity. OH and continuum emission as quantified by the Gaussian fit in the middle panel have been subtracted from the CO($J = 16\rightarrow15$) spectrum. The dashed gray histogram shows the CO($J = 5\rightarrow4$) emission (R10) for comparison, which demonstrates that the bulk of the CO($J = 16\rightarrow15$) line is covered by the 1.875 GHz bandpass shown.

(A color version of this figure is available in the online journal.)

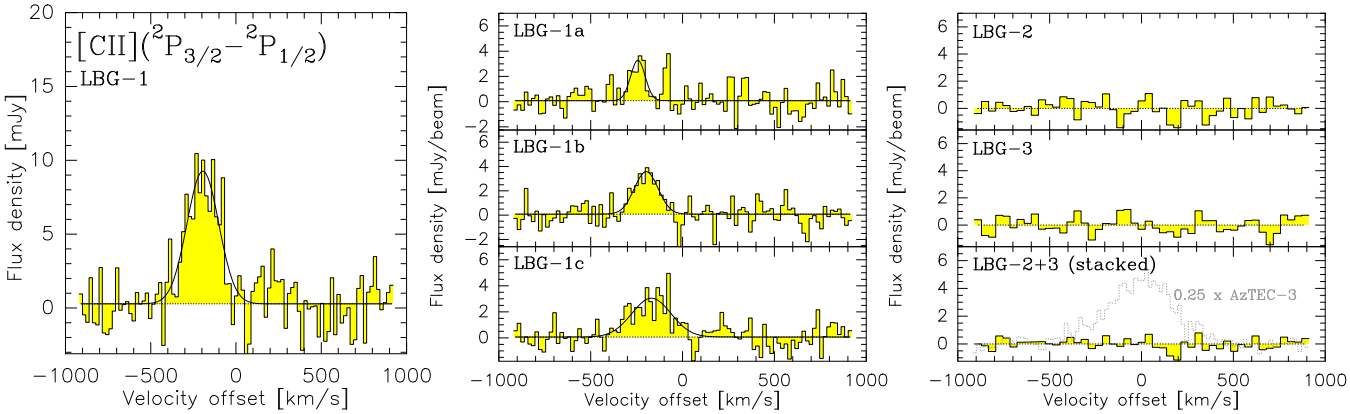

Figure 10. ALMA [C II]($^2P_{3/2}\rightarrow{}^2P_{1/2}$) spectra toward LBG-1 (left) and its components LBG-1a, LBG-1b, and LBG-1c (middle; see Figure 7), as well as LBG-2 and LBG-3 (right). Spectra (histograms) are shown at resolutions of 19.5 MHz (19 km s^{-1}; left and middle) or 39 MHz (39 km s^{-1}; right). The left spectrum corresponds to the spatially integrated emission shown as contours in Figure 7. The middle and right spectra are extracted at the optical peak positions for all sources (plus signs in Figures 1 and 7). The velocity scales are relative to $z = 5.2988$. Detected lines are shown along with Gaussian fits to the line emission (black curves). The bottom right panel shows a stack of the spectra of LBG-2 and LBG-3. The dashed gray histogram shows the [C II]($^2P_{3/2}\rightarrow{}^2P_{1/2}$) emission from the strong nearby source AzTEC-3 (Figure 9), scaled by a factor of 0.25, for comparison.

(A color version of this figure is available in the online journal.)

Table 3
[C II] Properties of LBG-1

Target	v_0[a] (km s^{-1})	d$v_{\rm C\,II}$ (km s^{-1})
LBG-1 (all components)	...	*218 ± 24*
LBG-1a	−49 ± 18	93 ± 32
LBG-1b	−3 ± 12	152 ± 29
LBG-1c	+25 ± 16	250 ± 41

Note. [a] Central line velocity relative to a redshift of 5.2950.

Table 4
Line Fluxes and Luminosities in AzTEC-3

	$I_{\rm line}$ (Jy km s^{-1})	$L'_{\rm line}$ (10^{10} K km s^{-1} pc^2)	Ref.
CO(J = 2→1)	0.23 ± 0.03	5.84 ± 0.78	1
CO(J = 5→4)	0.92 ± 0.09	3.70 ± 0.37	1
CO(J = 6→5)	1.36 ± 0.19	3.82 ± 0.54	1
CO(J = 16→15)	<0.22[a]	<0.09[a]	2
OH($^2\Pi_{1/2}$ J = 3/2→1/2)	1.44 ± 0.13	0.57 ± 0.05	2
[C II]($^2P_{3/2}$→$^2P_{1/2}$)	8.21 ± 0.29	3.05 ± 0.11	2

Notes. All quoted upper limits are 3σ.
[a] Assuming the same width as measured for the CO(J = 5→4) line (R10). Does not account for any uncertainty due to prior subtraction of OH emission (the closer OH component peaks ∼580 km s^{-1} redwards of the line).
References. (1) R10; (2) this work.

1.9 ± 0.3 is adopted for β. The best fit solution has a χ^2 of 19.44 for 10 degrees of freedom. We find $T_{\rm dust} = 52.8^{+5.0}_{-5.4}$ K, $\beta = 1.83 \pm 0.22$, and $\alpha = 6.64^{+2.56}_{-2.48}$, but we note that α is only poorly constrained by the data. The relatively high χ^2 reflects the fact that the routine experiences difficulties with simultaneously fitting the short- and long-wavelength data with the given set of parameters.

To improve the match, we also fit optically thick models, introducing the wavelength $\lambda_0 = c/\nu_0$ where the optical depth $\tau_\nu = (\nu/\nu_0)^\beta$ reaches unity as an additional fitting parameter. The best fit solution has a χ^2 of 14.63 for nine degrees of freedom, suggesting a significantly better fit than in the optically thin case. We find $\lambda_0 = 177^{+39}_{-38}$ μm (rest-frame wavelength). We also find $T_{\rm dust} = 88.4^{+9.8}_{-9.6}$ K, $\beta = 2.16 \pm 0.27$, and $\alpha = 6.17^{+2.73}_{-2.60}$. We caution that the uncertainties on the photometry close to the peak of the SED are >30%–50% (see also discussion by Huang et al. 2014; Smolčić et al. 2014), allowing for a broad range in possible peak wavelengths. The best fit solution yields an FIR luminosity of $L_{\rm FIR} = (1.10^{+0.22}_{-0.21}) \times 10^{13}$ $L_\odot$.[18] Assuming standard relations and a dust absorption coefficient of κ_ν = 2.64 m^{2}kg^{-1} at 125 μm (e.g., Dunne et al. 2003, their equation 1),[19] we also find a dust mass of $M_{\rm dust} = 2.66^{+0.74}_{-0.80} \times 10^8$ $M_\odot$.

3.4.2. Lyman-Break Galaxies

Given the detailed available photometry from COSMOS, we match galaxy templates to the observed SED of LBG-1 (see Figure 12, left). Fits are obtained by normalizing all templates to the observed Subaru i-band flux of the LBG (i.e., rest-frame ultraviolet light). Differences in photometry shortward of the Lyα line are not considered further in the comparison, since the nearby galaxy templates do not account for intergalactic medium absorption at $z = 5.3$ due to the Gunn–Peterson effect (Gunn & Peterson 1965). The ALMA continuum limit for LBG-1 is inconsistent with the SED shapes of spiral, starburst, and dust-obscured galaxies in the nearby universe, but is consistent with the flatter SED shapes typically observed in nearby dwarf galaxies. Similar results are found for LBG-2 and LBG-3 when assuming the same redshift as for LBG-1 (Figure 12, middle and right). To determine the $L_{\rm FIR}$ of LBG-1, we thus integrated the dwarf galaxy templates over their infrared peaks.[20] This results in $L_{\rm FIR}$ limits of <1.1–3.4 × 10^{11} $L_\odot$.[21] We conservatively scale the highest of these templates to the ALMA limits in the following. We then assume LBG-2 and LBG-3 to have the same redshift and SED shape as LBG-1 to determine limits on their $L_{\rm FIR}$.

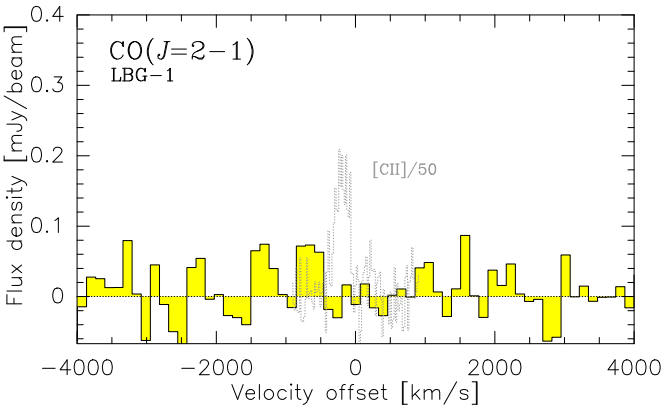

Figure 11. VLA spectrum covering the redshifted CO(J = 2→1) frequency toward LBG-1 (D. A. Riechers et al. 2015, in preparation). Spectrum (histogram) is shown at a resolution of 16 MHz (131 km s^{-1}). The velocity scale is relative to $z = 5.2988$. The dashed gray histogram shows the [C II]($^2P_{3/2}$→$^2P_{1/2}$) emission (Figure 10), scaled by a factor of 1/50, for comparison.
(A color version of this figure is available in the online journal.)

Based on the upper limit for the rest-frame 157.7 μm continuum flux density, we assume standard relations and the same dust absorption coefficient as for AzTEC-3 to place constraints on the dust mass of LBG-1. Assuming a dust temperature of $T_{\rm dust}$ = 30 K and an opacity power law index of β = 1.5 yields $M_{\rm dust}$<3.1–9.4 × 10^7 $M_\odot$,[22] where the range indicates the difference between point source and extended source limits.

3.5. Derivation of Further Galaxy Properties

We derive line luminosities from the observed [C II] intensities using standard relations (e.g., Solomon & vanden Bout 2005; Carilli & Walter 2013). We assume a Chabrier (2003) stellar initial mass function (IMF) to derive star formation rates from $L_{\rm FIR}$. For AzTEC-3, we use the measured continuum size to estimate the average star formation rate surface density. Based on the line width and [C II] galaxy sizes measured along the

[18] $L_{\rm FIR}$ is determined over the rest-frame 42.5–122.5 μm range throughout. Note that C11 determined $L_{\rm FIR}$ for AzTEC-3 over the rest-frame 60–120 μm range.
[19] The uncertainty in κ_ν is at least ∼0.4 dex.
[20] Corresponding to the rest-frame 42.5–122.5 μm range.
[21] We did not correct for effects due to the cosmic microwave background (CMB), which has a temperature of $T_{z,\rm CMB} \simeq 17$ K at the redshift of AzTEC-3 and LBG-1. Any corrections to the $L_{\rm FIR}$ limits required are small compared to other sources of uncertainty unless the dust temperature approaches $T_{z,\rm CMB}$ (see, e.g., da Cunha et al. 2013). The dust temperatures of the dwarf galaxies used as templates are $T_{\rm dust} \simeq$ 26–37 K (e.g., Israel et al. 1996b; Skibba et al. 2011), which would require corrections at the few percent level at most.
[22] These assumptions for $T_{\rm dust}$ and β are consistent with constraints obtained from stacking studies of LBGs at lower redshifts (e.g., Lee et al. 2012). Assuming $T_{\rm dust}$ = 25 or 40 K instead would yield ∼1.9× or ∼0.44× the quoted $M_{\rm dust}$ limit. Assuming β = 2.0 instead would yield a 12% higher limit for $M_{\rm dust}$, and thus, would have a minor impact compared to other sources of uncertainty.

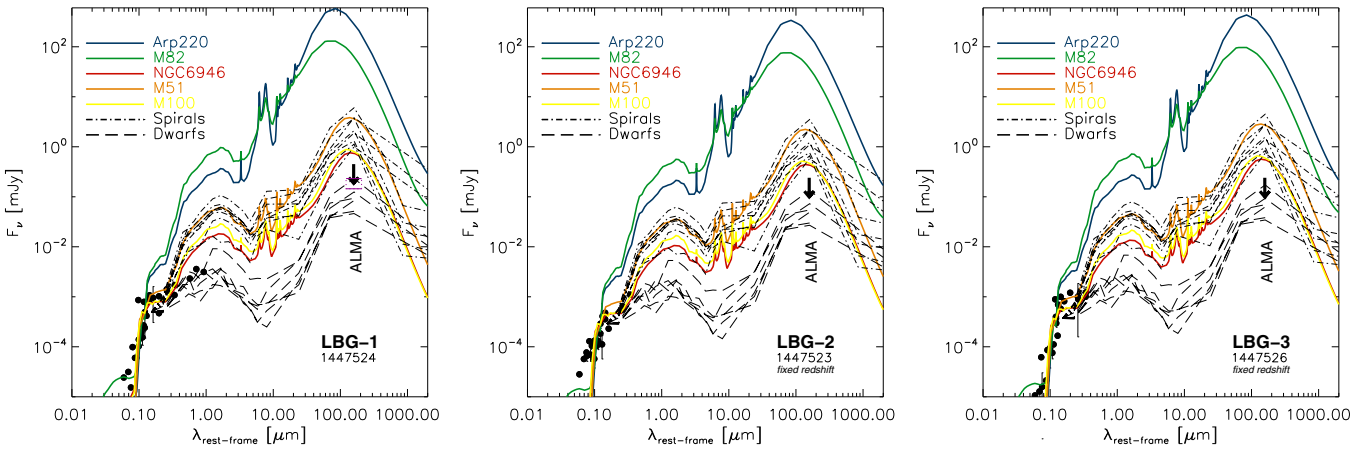

Figure 12. Spectral energy distributions of LBG-1, LBG-2, and LBG-3, and matched galaxy templates. The redshifts for LBG-2 and LBG-3 are assumed to be the same as measured for LBG-1. The templates for the nearby starburst and ultra-luminous infrared galaxies M51, M82, M100, NGC 6946, and Arp 220 (colored lines; Silva et al. 1998), the spirals NGC 1097, NGC 3351, NGC 5055, NGC 3031, NGC 7331, NGC 4736, and NGC 3627 (dot-dashed lines), and the dwarfs Holmberg I, NGC 6822, Holmberg II, DDO 053, IC 2574, and NGC 1705 (dashed lines; both samples from Dale et al. 2007) are normalized to the Subaru *i*-band fluxes of the LBGs. The arrows indicate the upper limits on the rest-frame 157.7 μm continuum flux obtained from our ALMA observations. The magenta bars in the left panel indicate the range of 157.7 μm point source limits for the subcomponents LBG-1a, LBG-1b, and LBG-1c.

(A color version of this figure is available in the online journal.)

major axis, we then use an isotropic virial estimator (e.g., Engel et al. 2010) to derive dynamical masses for all [C II]-detected sources (see Table 2).

4. ANALYSIS

4.1. The Massive Starburst Galaxy AzTEC-3

Despite its high $L_{\rm FIR}$, both the continuum and [C II] line emission in the massive starburst galaxy AzTEC-3 are fairly compact. The bulk of the atomic gas as traced by [C II] is distributed over a region of only $\lesssim$2 kpc radius.[23] In spite of the high signal-to-noise ratio (and thus, high centroid precision in the velocity channels in Figure 5) of our [C II] detection, there is no evidence for a significant velocity gradient on >1 kpc scales for the bulk of the emission. This suggests that the comparatively large velocity widths of the atomic and molecular lines are dominantly supported by emission from highly dispersed gas (the median [C II] velocity dispersion at the spatial resolution of our observations is $\sim$315 km s^{-1}), rather than ordered rotation. Only at faint levels do we find evidence for tidal structure or outflowing/infalling streams of gas. AzTEC-3 thus appears to be considerably more compact than some other $z > 4$ SMGs such as GN20 or HDF 850.1 ($\sim$4 times larger in the FIR continuum; Younger et al. 2008; Carilli et al. 2010; Walter et al. 2012a; Neri et al. 2014), but it is more comparable in extent to the $z = 6.34$ starburst HFLS3 (3.4 kpc $\times$ 2.9 kpc diameter in [C II], 2.6 kpc $\times$ 2.4 kpc diameter in the rest-frame 157.7 μm continuum; Riechers et al. 2013).

Based on the size of the far-infrared continuum emission ($\sim$2.1 kpc^2) and the star formation rate of 1100 $M_\odot$ yr^{-1}, we find a high star formation rate surface density of $\Sigma_{\rm SFR}$ = 530 $M_\odot$ yr^{-1} kpc^{-2} and a $L_{\rm FIR}$ surface density of $\Sigma_{\rm FIR}$ = 0.5 $\times$ 10^{13} $L_\odot$ kpc^{-2}. This is close to the theoretically predicted Eddington limit for starburst disks that are supported by radiation pressure, and is consistent with theories for so-called maximum starbursts (Elmegreen 1999; Scoville 2003; Thompson et al. 2005). Comparable, compact "hyper-starbursts" were found in the $z = 6.42$ quasar host galaxy J1148+5251, and in the $z = 6.34$ dusty galaxy HFLS3 ($\Sigma_{\rm SFR}$ = 1000 and 600 $M_\odot$ yr^{-1} kpc^{-2}; Walter et al. 2009; Riechers et al. 2013). Nearby, comparable $\Sigma_{\rm SFR}$ are only found in the very centers of GMCs or in the nuclei of ultra-luminous infrared galaxies like Arp 220.

The picture of a relatively compact, warm starburst is consistent with the molecular gas excitation in AzTEC-3, which is comparable to that in the similarly compact and warm $z = 6.34$ starburst HFLS3 (Riechers et al. 2013), but considerably higher than in other, less compact $z > 4$ SMGs like GN20 and HDF 850.1 (R10; Carilli et al. 2010; Walter et al. 2012a) and in typical $z \sim$ 2–3 SMGs (e.g., Riechers et al. 2011b, 2011c). The gas excitation in AzTEC-3, however, is lower than in quasar host galaxies, where the active galactic nucleus (AGN) may contribute to the excitation of high-level CO lines (e.g., Riechers et al. 2006, 2009, 2011a; Weiß et al. 2007). In particular, the nondetection of CO($J = 16\rightarrow15$) emission is consistent with no luminous AGN component contributing to the gas heating, in agreement with previous models of the CO excitation (R10). This picture is also consistent with the relatively low $L_{\rm C\,II}/L_{\rm FIR}$ ratio of 4.0 $\times$ 10^{-4}. This value is comparable to that of HFLS3 (5.4 $\times$ 10^{-4}; Riechers et al. 2013), and lower than in other, less compact $z > 4$ SMGs like HDF 850.1 (1.7 $\times$ 10^{-3}; Walter et al. 2012a), but higher than in some quasar host galaxies (e.g., 1.9 $\times$ 10^{-4} for J1148+5251; Walter et al. 2009). It is in agreement with the ($L_{\rm C\,II}/L_{\rm FIR}$)–$\Sigma_{\rm IR}$ relation for nearby infrared-luminous galaxies (Diaz-Santos et al. 2013). This ratio suggests the presence of a stronger-than-average far-UV radiation field due to a warm, dense, compact starburst with high $\Sigma_{\rm SFR}$, but gives no direct indication for the presence of an obscured AGN. Given the inferred compactness and high density of the gas and dust, it cannot be ruled out that the optical depth of the dust in AzTEC-3 at rest-frame 157.7 μm is considerable, and thus, that $L_{\rm C\,II}$ is comparatively low due to extinction. Using the $L_{\rm CO(1-0)}$ found from CO excitation modeling to CO($J = 2\rightarrow1$) and higher-J lines (R10), we find $L_{\rm C\,II}/L_{\rm CO(1-0)} \simeq$ 2070, which is by $\sim$50% lower than the value found for HFLS3 ($L_{\rm C\,II}/L_{\rm CO(1-0)} \simeq$ 3050; Riechers et al. 2013). This would be consistent with a higher

[23] This result is consistent with earlier estimates of the size of the molecular gas reservoir, which resulted in a limit of <4 kpc on the radius based on lower spatial resolution CO observations. Under the plausible assumption that the system is not dark matter dominated within its central few kiloparsec, a limit on the gas disk-equivalent radius of $r_0 < 2.3$ kpc was obtained (R10).

dust optical depth in AzTEC-3 compared to HFLS3, resulting in a reduced [C II] line luminosity. From our SED modeling, we find a dust optical depth of $\tau_{157.7\,\mu m} = 1.28 \pm 0.04$ at the wavelength of the [C II] emission for AzTEC-3, which is higher than what is found for HFLS3 ($\tau_{157.7\,\mu m} \lesssim 1$; Riechers et al. 2013). This suggests that, in contrast to HFLS3, the dust in AzTEC-3 is at least moderately optically thick toward [C II] line emission. Extinction of the [C II] line by dust would be consistent with the finding that this line may be somewhat narrower than the CO lines (421 ± 19 versus 487 ± 58 km s^{-1}; R10). However, it is important to point out that internal, differential gas excitation between different components within the galaxy could easily account for such a small, barely significant difference in line width as well. We do not correct the [C II] line luminosity for extinction, but we note that the above picture would remain essentially unchanged for even a factor of a few higher $L_{\rm C\,II}$.

The observed $L'_{\rm line}$ ratio, and thus, the brightness temperature ($T_{\rm b}$) ratio between the [C II]($^2P_{3/2} \rightarrow {}^2P_{1/2}$) and CO($J = 2 \rightarrow 1$) lines is 0.52 ± 0.07 (Table 4). Previous two-component CO excitation modeling suggests optical depths of $\tau_{\rm CO\,2-1} = 1.5$ and 35.9 for the low- and high-excitation gas components that are estimated to contribute 27.5% and 72.5% to the CO($J = 2 \rightarrow 1$) line luminosity, respectively (obtained from the models shown by R10), which implies that the CO emission is optically thick. Assuming that the [C II] and CO emission emerge from regions of similar surface area, the similarity in observed $T_{\rm b}$ would suggest that the [C II] line emission either is optically thick as well, or alternatively, that it has an intrinsically higher line excitation temperature than the CO emission ($T_{\rm ex}^{\rm CO\,2-1} = 18.3$ and 44.9 K at kinetic temperatures of $T_{\rm kin} = 30$ and 45 K for the low- and high-excitation gas components in the model of R10). The latter may be expected if a large fraction of the [C II] emission is associated with PDRs (e.g., Stacey et al. 2010).

Finally, the detection of strong OH($^2\Pi_{1/2}\ J = 3/2 \rightarrow 1/2$) emission at almost 20% of the [C II] line luminosity is also consistent with a warm starburst with an intense radiation field. The high upper level energy and high critical density of this transition ($E_{\rm up}/k_{\rm B} \simeq 270$ K and $n_{\rm crit} \simeq 10^{8.6}$ cm^{-3}, respectively) makes collisional excitation unlikely, but instead indicates the presence of a strong infrared radiation field. This is consistent with what was found for the $z = 6.34$ dusty starburst HFLS3, the only other high-z galaxy detected in the 163 μm OH doublet to date (Riechers et al. 2013). The slight blueshift of the OH feature relative to the CO and [C II] lines in AzTEC-3 would be consistent with the presence of a molecular outflow.

We find a molecular gas mass fraction of $f_{\rm gas} = M_{\rm H_2}/M_{\rm dyn} \simeq 55\%$, with $\sim$10% of $M_{\rm dyn}$ being due to stellar mass. Taken at face value, this would indicate that $\lesssim$35% of the mass of AzTEC-3 in the central $\sim$4 kpc are due to dark matter. Conversely, even if no dark matter were to be present, these considerations place an upper limit on the CO luminosity to gas mass conversion factor of $\alpha_{\rm CO} < 1.3\ M_\odot\ ({\rm K\,km\,s^{-1}\,pc^2})^{-1}$, which is $\sim$3$\times$ lower than the Galactic $\alpha_{\rm CO}$.[24] Using $\alpha_{\rm CO} = 0.8\ (<1.3)\ M_\odot\ ({\rm K\,km\,s^{-1}\,pc^2})^{-1}$, we find a gas-to-dust mass ratio of $M_{\rm H_2}/M_{\rm dust} \simeq 200\ (<330)$, i.e., $\sim$3$\times$ higher than in HFLS3 when assuming the same $\alpha_{\rm CO}$ (Riechers et al. 2013). These values are higher than the average of 120 ± 28 found for the nuclei of nearby infrared-luminous galaxies, but within the range of values measured for individual sources (29–725; Wilson et al. 2008).

[24] The original molecular gas mass estimate of $5.3 \times 10^{10}\ M_\odot$ assumed $\alpha_{\rm CO} = 0.8\ M_\odot\ ({\rm K\,km\,s^{-1}\,pc^2})^{-1}$ for AzTEC-3 (R10).

AzTEC-3, as the most massive, most intensely star-forming galaxy in the protocluster, thus is a compact, gas-dominated galaxy that hosts a maximal starburst. Its relative compactness, and implied high $\Sigma_{\rm SFR}$ appear not to be a common feature among $z > 4$ SMGs, but are comparable to the most extreme other cases known. In particular, the $z = 4.05$ galaxy GN20, which is also associated with an overdensity of galaxies (Daddi et al. 2009), is significantly more extended by a factor of a few and has lower $\Sigma_{\rm SFR}$ and lower molecular gas excitation (e.g., Carilli et al. 2010). The $z = 5.18$ SMG HDF 850.1 is also associated with an (less pronounced) overdensity of galaxies, is significantly more extended by a factor of a few, and has lower $\Sigma_{\rm SFR}$ and lower molecular gas excitation than AzTEC-3 (Walter et al. 2012a). Assuming that these systems are the progenitors of the same population of massive central cluster galaxies, AzTEC-3 thus appears to be in a different phase of its evolution. This makes it particularly interesting to further understand how this may be connected to the properties of its environment.

4.2. The Lyman-Break Galaxies (LBGs)

We solidly detect and spatially resolve [C II] emission in the "typical" $z > 5$ star-forming system LBG-1. The atomic gas is spatially and dynamically resolved toward all three optically identified sources. We resolve at least two major velocity gradients between the different components (Figure 7). The smaller gradient appears to be associated with the northern component LBG-1c. The larger gradient appears to extend from the southern component LBG-1a across the middle component LBG-1b toward LBG-1c (blue- to redshifted emission), but it may mask smaller-scale gradients associated with the individual components at the present spatial resolution. In particular, there is tentative evidence for smaller-scale velocity gradients with opposing directions, pointing from the "overlap" region in between LBG-1a and LBG-1b towards the centers of the two optical sources, but higher spatial resolution is required to confirm and more clearly separate these smaller-scale gradients.[25] This system thus may represent a merger of three Lyman-break galaxies, or some other form of complex, clumpy, extended system in formation. The dynamical mass of the triple system is about half that of the SMG AzTEC-3 (Table 2), showing that LBG-1 contributes a significant fraction of the mass bound in galaxies to the protocluster environment.

The [C II] emission integrated over all components is $\sim$4$\times$ fainter than in the SMG AzTEC-3, suggesting that each of the components is typically by about an order of magnitude fainter than the SMG. There is no evidence for continuum emission at the position of LBG-1, suggesting that it is at least $\gtrsim$15$\times$ fainter (>25–40$\times$ fainter for the individual subcomponents) than the SMG (3σ). Assuming an SED shape similar to AzTEC-3, this would suggest an SFR of ${\rm SFR_{FIR}} < 80\ M_\odot\ {\rm yr^{-1}}$ ($\lesssim$25–40 $M_\odot$ yr^{-1} for the subcomponents). From the [C II] luminosity, we obtain an estimate of ${\rm SFR_{FIR}} \sim 150\ M_\odot\ {\rm yr^{-1}}$, using the relation for dusty starbursts recently suggested by Sargsyan et al. (2012). This is somewhat inconsistent with the continuum-based estimate, unless a bottom-heavy IMF is assumed (e.g., Conroy & van Dokkum 2012). However, despite the limited constraints on the rest-frame far-infrared SED of the source,

[25] Note that the spatial separation of the optical components in LBG-1 is not much larger than the synthesized beam size of our observations, but the centroid positions in individual velocity channel maps are known to significantly higher precision than the beam size at the given signal-to-noise ratio. This enables studies of velocity gradients on smaller scales than the beam size.

typical spiral/starburst and dusty galaxy SED templates can be ruled out to fit the SED of LBG-1 (Figure 12). Templates for dwarf galaxies provide a substantially better match to the overall SED, suggesting that LBG-1 is not a (very) dusty system, and providing an upper limit to the SFR of $SFR_{FIR} < 18$–$54\ M_\odot\ yr^{-1}$ (the range represents the difference between point source and extended source limits, since the actual limit depends on the size of the emitting region; see Table 2). We consider this to be the currently best estimate for the FIR SFR in this system. From the range of templates that best represent the data, the possibility of a comparatively low, sub-solar metallicity cannot be excluded as an important reason for the low implied FIR flux of the system. However, the detection of strong 157.7 μm [C II] emission and the presence of deep interstellar metal absorption features in rest-frame UV spectra (C11) is inconsistent with very low metallicities. We thus consider it most likely that the SED shape is due to the combination of a young starburst and some contribution of optical light from a stellar population that is already in place. In particular, the lack of a strong "bump" at rest-frame optical wavelengths (relative to the strength of the rest-frame UV emission that is dominated by young, massive stars) may indicate the lack of a significant older stellar population. Such a scenario is consistent with what is expected for a young, recently formed galaxy observed at an early cosmic epoch, only 1.1 billion years after the Big Bang. We independently estimated the star formation rate based on the rest-frame UV continuum emission of the galaxy (e.g., Madau et al. 1998), using the SED fitting methods outlined by C11. This yields $SFR_{UV} = 22\ M_\odot\ yr^{-1}$. This is comparable to the best SFR_{FIR} limit, and again consistent with low dust extinction. By assuming $SFR_{total} = SFR_{UV}+SFR_{FIR}$, we find that at most <45%–71% of the star formation activity in LBG-1 is obscured by dust. The UV-to-optical SED shape is consistent with a dust extinction of only $A_V \simeq 0.5$ mag (C11). The finding of low dust extinction is consistent with recent estimates for LBGs at comparable and higher redshifts in the rest–frame optical (e.g., Bouwens et al. 2010), suggesting that detection of such galaxies in the FIR continuum may require substantial integration times even with ALMA. This is also consistent with recent, less sensitive far-infrared studies of Lyman-α emitters (Walter et al. 2012b; Gonzalez-Lopez et al. 2014). Given its stellar mass (C11) and total star formation rate, LBG-1 is consistent with being situated on the star-forming "main sequence" at $z \approx 5$ (e.g., Speagle et al. 2014).

From the [C II] luminosity and L_{FIR} limit, we find an $L_{C\,II}/L_{FIR}$ limit of $>3.1 \times 10^{-3}$ to $>9.4 \times 10^{-3}$ (the higher limit applies if the far-infrared continuum emission is not resolved by our observations), i.e., approximately >0.3% to >0.9%. This is consistent with normal, star-forming galaxies at low redshift, but significantly higher than in dusty quasars and extreme starburst galaxies (e.g., Gracia-Carpio et al. 2011; Diaz-Santos et al. 2013). Assuming thermalized excitation between CO($J = 2 \rightarrow 1$) and CO($J = 1 \rightarrow 0$), we find a $L_{C\,II}/L_{CO(1-0)}$ limit of >4600. This is consistent with a comparatively modest UV radiation field strength (e.g., Stacey et al. 2010), comparable to normal, star-forming galaxies in the local universe when accounting for the reduction in CO($J = 2 \rightarrow 1$) luminosity due to the CMB at the redshift of LBG-1.[26]

Our findings are consistent with the assumption that the protocluster member LBG-1 is a "typical," close to $L^\star_{UV}$ star-forming system at $z > 5$ with relatively low dust content. LBG-1 appears to be a triple system, but our sensitivity would have been sufficient to pick up a single component with one-third of the [C II] luminosity within the protocluster. We thus conclude that LBG-2 and LBG-3, which have photometric redshifts/colors consistent with the protocluster environment, either have [C II] luminosities that are lower than those of the individual components of LBG-1 by at least a factor of three (which would be consistent with their UV/optical properties within the relative uncertainties), or have redshifts outside of our bandpass ($dz \simeq 0.04$ per 1.875 GHz band). Independent spectroscopic confirmation and/or more sensitive [C II] observations will be required to distinguish between these possibilities. Note that eight additional LBGs identified as likely protocluster members at larger distances from the center (C11) were not covered by this initial investigation, and thus, could have higher [C II] and/or FIR luminosities than LBG-1.

5. DISCUSSION AND CONCLUSIONS

We have detected [C II] emission toward the intensely star-forming SMG (AzTEC-3) and a triple Lyman-break galaxy system (LBG-1) associated with the $z = 5.3$ AzTEC-3 protocluster environment (C11, R10). These member galaxies lie within a redshift range of $dz < 0.004$, suggesting that the association of galaxies is not only close in the sky plane, but along the line of sight as well. We further detected OH($^2\Pi_{1/2}$ $J = 3/2 \rightarrow 1/2$) line and rest-frame 157.7 μm continuum emission in the SMG AzTEC-3, and placed a stringent limit on its CO($J = 16 \rightarrow 15$) luminosity. Our observations are consistent with a relatively compact (~2.5 kpc diameter), highly dispersed, warm, "maximum starburst" in its peak phase in the massive galaxy AzTEC-3, with possible evidence for outflowing gas from the star-forming regions, and/or tidal structure. There is no evidence for an AGN contribution to the excitation of the gas. Its overall properties are reminiscent of the most extremely active massive, dusty starburst galaxies found within the (general) SMG population (e.g., Riechers et al. 2013). Our observations are also consistent with LBG-1 being a "typical," close to $L^\star_{UV}$ galaxy following the star-forming "main sequence" at its cosmic epoch, with little evidence for old stellar populations or the presence of dust. LBG-1 is not detected in sensitive CO or far-infrared continuum observations, which is consistent with what is expected for a young starburst with perhaps subsolar metallicity. LBG-1 shows a complex kinematic structure, perhaps representing a merger of three smaller galaxies. Using only a fraction of the full ALMA science array, we thus detect and spatially resolve the interstellar medium in both distant massive starbursts and "typical" $z > 5$ star-forming galaxies at relative ease. We, however, do not detect two fainter candidate members of the protocluster, which suggests that they either are an order of magnitude fainter in [C II] emission than LBG-1, or that their systemic redshifts fall outside the range covered by our observations. The capabilities of ALMA in a more advanced stage of completion will be necessary to further address this issue.

The detection of [C II] emission in LBG-1 is interesting for a number of reasons. Recent searches for [C II] emission in $z > 6.5$ Lyα emitters (LAEs) and Lyα blobs (LABs) have been unsuccessful, even with ALMA (e.g., Walter et al. 2012b; Ouchi et al. 2013; Gonzalez-Lopez et al. 2014). These systems have SFR_{UV} that are comparable to LBG-1, and even exceed it by a factor of a few in the most extreme cases, but they remain undetected in [C II] emission down to comparable, and sometimes deeper levels than required to detect LBG-1. The successful detection of LBG-1 may suggest that this

[26] We here assume a moderate gas kinetic temperature of $T_{kin} \sim 30$ K, and that the CO($J = 2 \rightarrow 1$) emission is optically thick.

is a selection effect. The difference in cosmic time between the redshift of LBG-1 and $z = 6.5$ is only ~250 Myr. As such, it is not clear that the earlier epochs in which the LAEs and LABs were observed are the main deciding factor. We consider it more likely that the narrowband Lyα selection technique that has led to the initial identification of the LAEs and LABs targeted in [C II] emission at $z > 6.5$ selects against galaxies with sufficient metallicity, and thus carbon abundance, to produce enough [C II] line flux to be detectable. This is consistent with the detection of [C II] emission in other, albeit significantly more active and massive star-forming galaxy populations at comparable redshifts (e.g., Riechers et al. 2013). Gonzalez-Lopez et al. (2014) have suggested that high-redshift galaxies with high UV continuum fluxes but low Lyα equivalent widths may be more likely to have sufficient metallicity to be detectable in the [C II] line. This is consistent with the [C II] detection of LBG-1, which has a comparatively low Lyα equivalent width (C11). In any case, our study shows that, even if the detection of dust in "typical" galaxies at very high redshift may require substantial integration times, their gas content appears to be detectable with ALMA in the [C II] line using only moderate amounts of observing time, with the possible exception of systems with the lowest metallicities (cf. Fisher et al. 2014).

It is also interesting to discuss the properties of LBG-1 in the context of the BR 1202–0725 system at $z = 4.69$. This system consists of two far-infrared-luminous (each $>10^{13}\,L_\odot$), massive galaxies, separated by 26 kpc in projection, one of which is an optically luminous broad absorption line quasar. Early ALMA observations have revealed two faint [C II]-emitting sources in close proximity to the quasar (<15 kpc in projection), which appear to be associated with LAEs (components Lyα-1 and Lyα-2; e.g., Wagg et al. 2012; Carilli et al. 2013). These LAEs, however, have very large Lyα equivalent widths due to Lyα lines with $>1200\,\mathrm{km\,s^{-1}}$ FWHM (e.g., Williams et al. 2014). Given the strong tidal forces, and perhaps ongoing interaction between the two massive galaxies, the close proximity and characteristics of these LAEs thus have likely implications for the evolution (e.g., besides its strong radiation field, the quasar shows a possible outflow in the direction of one of the LAEs), and perhaps even the origin of these sources (e.g., it cannot be ruled out that they represent, or formed out of, tidal debris from the massive galaxies). As such, it is unclear to what degree the LAEs in this system can be considered "typical" galaxies. However, given the lack of detections of "typical" high-redshift galaxies in [C II] emission prior to our study, and since these LAEs are significantly less extreme than all other systems detected in [C II] at high redshift, it is instructive to compare the properties of LBG-1 to those of the LAEs in BR 1202–0725 (we adopt their properties from the study of Carilli et al. 2013 below).

In contrast to LBG-1, the Lyα-2 component in the BR 1202–0725 system is detected in the far-infrared continuum, suggesting a FIR luminosity in excess of $10^{12}\,L_\odot$. Only part of the [C II] line in Lyα-2 is detected at the edge of the bandpass, indicating a line FWHM of $>338\,\mathrm{km\,s^{-1}}$. This suggests that the line is significantly broader than in LBG-1 (which has a total FWHM of $218 \pm 24\,\mathrm{km\,s^{-1}}$; Table 1). Ly$\alpha$-2 has an $L_{\mathrm{C\,II}}/L_{\mathrm{FIR}}$ ratio of $>5 \times 10^{-4}$. Assuming that at least half the [C II] line in Lyα-2 is covered by the bandpass, this suggests an at least $\gtrsim$3–10× lower ratio than in LBG-1. These properties are consistent with Lyα-2 being a luminous, dusty starburst system, perhaps not representative of $L^\star_{\mathrm{UV}}$ galaxies at $z \sim 4.7$, but less extreme than other dusty starbursts at high redshift detected in [C II] previously.

The Lyα-1 component in the BR 1202–0725 system is not detected in the far-infrared continuum, implying $L_{\mathrm{C\,II}}/L_{\mathrm{FIR}} > 5 \times 10^{-4}$. This limit is by about an order of magnitude lower than that in LBG-1. It thus remains unclear how its $L_{\mathrm{C\,II}}/L_{\mathrm{FIR}}$ compares to normal, star-forming galaxies nearby. The [C II] line in Lyα-1 has an FWHM of only $56 \pm 11\,\mathrm{km\,s^{-1}}$, corresponding to ~4% of the width of its Lyα line (Williams et al. 2014). This also corresponds to ~60% of the width of LBG-1a, i.e., the narrowest component of LBG-1. As discussed by Carilli et al. (2013), it remains unclear if Lyα-1 is a physically distinct system, or a local maximum in a tidal "bridge" connecting the massive, far-infrared-luminous galaxies. In any case, based on the existing constraints, the properties of Lyα-1 and LBG-1 appear to be quite dissimilar as well, but more detailed ALMA data on the BR 1202–0725 system will be required to further investigate possible similarities.

It remains to be seen what role the environment plays in the evolution of LBG-1. To address this issue in more detail, a first step will be a complete study of the AzTEC-3 protocluster with ALMA (the current study only covered the center of the region) and similar environments to be discovered in the future. Equally importantly, sensitive studies of "blank fields" in the [C II] emission line will be necessary for an unbiased investigation of the [C II] luminosity function (an approximate, but independent measure of the atomic gas content of galaxies through cosmic times), and to properly constrain the "hidden," dust-obscured part of the star formation history of the universe through the detection of previously unknown faint, dusty star-forming galaxies. Such C^+ deep fields will be an important complement to similar studies in CO and continuum emission alone (studies of [C II] in continuum-preselected samples will only yield a biased view of this issue; e.g., Swinbank et al. 2012).

When ALMA is completed in the coming months, it will be an ideal tool for the most sensitive of these investigations. Given the relative strength of the [C II] line, CCAT will be able to detect [C II] emission over regions the size of the AzTEC-3 protocluster in a single shot using multi-object spectroscopy by the end of the decade. Ultimately, CCAT will also enable complementing, large-area C^+ blank field studies that may cover regions as large as the full COSMOS field to appreciable depth.

We thank the anonymous referee for a helpful and constructive report, Jim Braatz for assistance with setting up the observations, Mark Lacy for taking on the QA2 check of the data, and Alex Conley for help with the SED fitting. The National Radio Astronomy Observatory is a facility of the National Science Foundation operated under cooperative agreement by Associated Universities, Inc. This paper makes use of the following ALMA data: ADS/JAO.ALMA# 2011.0.00064.S. ALMA is a partnership of ESO (representing its member states), NSF (USA) and NINS (Japan), together with NRC (Canada) and NSC and ASIAA (Taiwan), in cooperation with the Republic of Chile. The Joint ALMA Observatory is operated by ESO, AUI/NRAO and NAOJ. F.B. and A.K. acknowledge support from Collaborative Research Centre 956, sub-project A1, funded by the Deutsche Forschungsgemeinschaft (DFG). V.S. acknowledges support by the European Union's Seventh Framework program under grant agreement 337595 (ERC Starting Grant, "Cos-Mass"). Additional support for this work was provided by the NSF through award SOSPA0-002 from the NRAO.

REFERENCES

Blain, A. W., Chapman, S. C., Smail, I., & Ivison, R. 2004, ApJ, 611, 725
Blain, A. W., Smail, I., Ivison, R. J., Kneib, J.-P., & Frayer, D. T. 2002, PhR, 369, 111
Bouwens, R. J., Illingworth, G. D., Oesch, P. A., et al. 2010, ApJL, 708, L69
Capak, P. L., Riechers, D. A., Scoville, N. Z., et al. 2011, Natur, 470, 233 (C11)
Carilli, C. L., Daddi, E., Riechers, D., et al. 2010, ApJ, 714, 1407
Carilli, C. L., Riechers, D., Walter, F., et al. 2013, ApJ, 763, 120
Carilli, C. L., & Walter, F. 2013, ARA&A, 51, 105
Cesaroni, R., & Walmsley, C. M. 1991, A&A, 241, 537
Chabrier, G. 2003, PASP, 115, 763
Chapman, S. C., Blain, A. W., Ivison, R. J., & Smail, I. R. 2003, Natur, 422, 695
Condon, J. J. 1997, PASP, 109, 166
Conroy, C., & van Dokkum, P. G. 2012, ApJ, 760, 71
da Cunha, E., Groves, B., Walter, F., et al. 2013, ApJ, 766, 13
Daddi, E., Dannerbauer, H., Stern, D., et al. 2009, ApJ, 694, 1517
Dale, D. A., Gil de Paz, A., Gordon, K. D., et al. 2007, ApJ, 655, 863
Diaz-Santos, T., Armus, L., Charmandaris, V., et al. 2013, ApJ, 774, 68
Dowell, C. D., Conley, A., Glenn, J., et al. 2014, ApJ, 780, 75
Dunne, L., Eales, S. A., & Edmunds, M. G. 2003, MNRAS, 341, 589
Dwek, E., Staguhn, J. G., Arendt, R. G., et al. 2011, ApJ, 738, 36
Efstathiou, G., & Rees, M. J. 1988, MNRAS, 230, 5
Elmegreen, B. G. 1999, ApJ, 517, 103
Engel, H., Tacconi, L. J., Davies, R. I., et al. 2010, ApJ, 724, 233
Fisher, D. B., Bolatto, A. D., Herrera-Camus, R., et al. 2014, Natur, 505, 186
Genzel, R., Crawford, M. K., Townes, C. H., & Watson, D. M. 1985, ApJ, 297, 766
Gonzalez-Alfonso, E., Fischer, J., Gracia-Carpio, J., et al. 2012, A&A, 541, A4
Gonzalez-Lopez, J., Riechers, D. A., Decarli, R., et al. 2014, ApJ, 784, 99
Gracia-Carpio, J., Sturm, E., Hailey-Dunsheath, S., et al. 2011, ApJL, 728, L7
Gunn, J. E., & Peterson, B. A. 1965, ApJ, 142, 1633
Huang, J.-S., Rigopoulou, D., Magdis, G., et al. 2014, ApJ, 784, 52
Hughes, D. H., Serjeant, S., Dunlop, J., et al. 1998, Natur, 394, 241
Ilbert, O., Capak, P., Salvato, M., et al. 2009, ApJ, 690, 1236
Israel, F. P., Bontekoe, T. R., & Kester, D. J. M. 1996, A&A, 308, 723
Israel, F. P., Maloney, P. R., Geis, N., et al. 1996, ApJ, 465, 738
Kanekar, N., Wagg, J., Chary, R.-R., & Carilli, C. L. 2013, ApJL, 771, L20
Kauffmann, G., Colberg, J. M., Diaferio, A., & White, S. D. M. 1999, MNRAS, 307, 529
Lee, K.-S., Alberts, S., Atlee, D., et al. 2012, ApJL, 758, L31
Madau, P., Pozzetti, L., & Dickinson, M. 1998, ApJ, 498, 106
Maiolino, R., Caselli, P., Nagao, T., et al. 2009, A&A, 500, L1
Maiolino, R., Cox, P., Caselli, P., et al. 2005, A&A, 440, L51
McCracken, H. J., Milvang-Jensen, B., Dunlop, J., et al. 2012, A&A, 544, A156
McKee, C. F., & Ostriker, J. P. 1977, ApJ, 218, 148
Neri, R., Downes, D., Cox, P., & Walter, F. 2014, A&A, 562, A35
Ouchi, M., Ellis, R., Ono, Y., et al. 2013, ApJ, 778, 102
Riechers, D. A., Bradford, C. M., Clements, D. L., et al. 2013, Natur, 496, 329
Riechers, D. A., Capak, P. L., Carilli, C. L., et al. 2010, ApJL, 720, L131 (R10)
Riechers, D. A., Carilli, C. L., Maddalena, R. J., et al. 2011a, ApJL, 739, L32
Riechers, D. A., Carilli, C. L., Walter, F., et al. 2011b, ApJL, 733, L11
Riechers, D. A., Hodge, J., Walter, F., Carilli, C. L., & Bertoldi, F. 2011c, ApJL, 739, L31
Riechers, D. A., Walter, F., Bertoldi, F., et al. 2009, ApJ, 703, 1338
Riechers, D. A., Walter, F., Carilli, C. L., et al. 2006, ApJ, 650, 604
Sanders, D. B., Salvato, M., Aussel, H., et al. 2007, ApJS, 172, 86
Sargsyan, L., Lebouteiller, V., Weedman, D., et al. 2012, ApJ, 755, 171
Scott, K. S., Austermann, J. E., Perera, T. A., et al. 2008, MNRAS, 385, 2225
Scoville, N. 2003, JKAS, 36, 167
Scoville, N., Aussel, H., Brusa, M., et al. 2007, ApJS, 172, 1
Silva, L., Granato, G. L., Bressan, A., & Danese, L. 1998, ApJ, 509, 103
Skibba, R. A., Engelbracht, C. W., Dale, D., et al. 2011, ApJ, 738, 89
Smail, I., Ivison, R. J., & Blain, A. W. 1997, ApJL, 490, L5
Smolčić, V., Karim, A., Miettinen, O., et al. 2014, A&A, submitted
Solomon, P. M., & Vanden Bout, P. A. 2005, ARA&A, 43, 677
Speagle, J. S., Steinhardt, C. L., Capak, P. L., & Silverman, J. D. 2014, ApJS, 214, 15
Spergel, D. N., Bean, R., Doré, O., et al. 2007, ApJS, 170, 377
Spergel, D. N., Verde, L., Peiris, H. V., et al. 2003, ApJS, 148, 175
Spoon, H. W. W., Farrah, D., Lebouteiller, V., et al. 2013, ApJ, 775, 127
Springel, V., White, S. D. M., Jenkins, A., et al. 2005, Natur, 435, 629
Stacey, G. J., Geis, N., Genzel, R., et al. 1991, ApJ, 373, 423
Stacey, G. J., Hailey-Dunsheath, S., Ferkinhoff, C., et al. 2010, ApJ, 724, 957
Sturm, E., González-Alfonso, E., Veilleux, S., et al. 2011, ApJL, 733, L16
Swinbank, A. M., Karim, A., Smail, I., et al. 2012, MNRAS, 427, 1066
Thompson, T. A., Quataert, E., & Murray, N. 2005, ApJ, 630, 167
Valtchanov, I., Virdee, J., Ivison, R. J., et al. 2011, MNRAS, 415, 3473
Wagg, J., Carilli, C. L., Wilner, D. J., et al. 2010, A&A, 519, L1
Wagg, J., Wiklind, T., Carilli, C. L., et al. 2012, ApJL, 752, L30
Wang, R., Wagg, J., Carilli, C. L., et al. 2013, ApJ, 773, 44
Walter, F., Decarli, R., Carilli, C., et al. 2012a, Natur, 486, 233
Walter, F., Decarli, R., Carilli, C., et al. 2012b, ApJ, 752, 93
Walter, F., Riechers, D., Cox, P., et al. 2009, Natur, 457, 699
Weiß, A., Downes, D., Neri, R., et al. 2007, A&A, 467, 955
Williams, R. J., Wagg, J., Maiolino, R., et al. 2014, MNRAS, 439, 2096
Wilson, C. D., Petitpas, G. R., Iono, D., et al. 2008, ApJS, 178, 189
Younger, J. D., Fazio, Giovanni, G., Wilner, D. J., et al. 2008, ApJ, 688, 59